AFRL-RX-TY-TR-2011-0069

FUNCTIONALIZED NANO AND MICRO STRUCTURED COMPOSITE COATINGS (FINAL REPORT)

Igor Luzinov and Konstantin Kornev

School of Materials Science and Engineering
161 Sirrine Hall
Clemson University
Clemson, SC 29634-0971

June 2011

**AIR FORCE RESEARCH LABORATORY
MATERIALS AND MANUFACTURING DIRECTORATE**

■ **Air Force Materiel Command** ■ **United States Air Force** ■ **Tyndall Air Force Base, FL 32403-5323**

DISCLAIMER

NOTICE AND SIGNATURE PAGE

Using Government drawings, specifications, or other data included in this document for any purpose other than Government procurement does not in any way obligate the U.S. Government. The fact that the Government formulated or supplied the drawings, specifications, or other data does not license the holder or any other person or corporation; or convey any rights or permission to manufacture, use, or sell any patented invention that may relate to them.

This report was cleared for public release by the 88th Air Base Wing Public Affairs Office at Wright Patterson Air Force Base, Ohio and is available to the general public, including foreign nationals. Copies may be obtained from the Defense Technical Information Center (DTIC) (http://www.dtic.mil).

AFRL-RX-TY-TR-2011-0069 HAS BEEN REVIEWED AND IS APPROVED FOR PUBLICATION IN ACCORDANCE WITH ASSIGNED DISTRIBUTION STATEMENT.

JEFFERY R. OWENS, PhD
Work Unit Manager

MICHAEL V. HENLEY, DR-III
Chief, Airbase Sciences Branch

ALBERT N. RHODES, PhD
Chief, Airbase Technologies Division

This report is published in the interest of scientific and technical information exchange, and its publication does not constitute the Government's approval or disapproval of its ideas or findings.

REPORT DOCUMENTATION PAGE

*Form Approved
OMB No. 0704-0188*

The public reporting burden for this collection of information is estimated to average 1 hour per response, including the time for reviewing instructions, searching existing data sources, gathering and maintaining the data needed, and completing and reviewing the collection of information. Send comments regarding this burden estimate or any other aspect of this collection of information, including suggestions for reducing the burden, to Department of Defense, Washington Headquarters Services, Directorate for Information Operations and Reports (0704-0188), 1215 Jefferson Davis Highway, Suite 1204, Arlington, VA 22202-4302. Respondents should be aware that notwithstanding any other provision of law, no person shall be subject to any penalty for failing to comply with a collection of information if it does not display a currently valid OMB control number.
PLEASE DO NOT RETURN YOUR FORM TO THE ABOVE ADDRESS.

1. REPORT DATE *(DD-MM-YYYY)*	2. REPORT TYPE	3. DATES COVERED *(From - To)*
30-JUN-2011	Final Technical Report	21-MAY-2009 -- 31-MAY-2011

4. TITLE AND SUBTITLE	5a. CONTRACT NUMBER
Functional Polymeric Materials - from Research Labs to Field Applications: Functionalized Nano and Micro Structured Composite Coatings	FA8650-09-D-5900-0001

5b. GRANT NUMBER

5c. PROGRAM ELEMENT NUMBER
0602102F

6. AUTHOR(S)	5d. PROJECT NUMBER
Luzinov, Igor; Kornev, Konstantin	4915

5e. TASK NUMBER
L0

5f. WORK UNIT NUMBER
QL102009

7. PERFORMING ORGANIZATION NAME(S) AND ADDRESS(ES)	8. PERFORMING ORGANIZATION REPORT NUMBER
School of Materials Science and Engineering 161 Sirrine Hall, Clemson University Clemson, SC 29634-0971	

9. SPONSORING/MONITORING AGENCY NAME(S) AND ADDRESS(ES)	10. SPONSOR/MONITOR'S ACRONYM(S)
Air Force Research Laboratory Materials and Manufacturing Directorate Airbase Technologies Division 139 Barnes Drive, Suite 2 Tyndall Air Force Base, FL 32403-5323	AFRL/RXQL
	11. SPONSOR/MONITOR'S REPORT NUMBER(S)
	AFRL-RX-TY-TR-2011-0069

12. DISTRIBUTION/AVAILABILITY STATEMENT

Distribution Statement A: Approved for public release; distribution unlmited.

13. SUPPLEMENTARY NOTES

Ref Public Affairs Case # 88ABW-2011, 30 November 2011. Document contains color images.

14. ABSTRACT

Current methods of decontaminating Chemical Warfare Agents (CWA) contaminated equipment need significant improvement. To this end, the major objective of this work was to conduct research on development of effective nano and micro structured composite coatings capable to collect and decontaminate the chemical agents. In addition, the coating is intended to minimize the contamination cross-section of a coated vehicle. During the project we developed major components required to build effective protecting coatings against CWA. As a result of the work conducted several types of low-surface-energy coatings were created.

15. SUBJECT TERMS

coating, phobic, repellent, CWA, CARC.

16. SECURITY CLASSIFICATION OF:			17. LIMITATION OF ABSTRACT	18. NUMBER OF PAGES	19a. NAME OF RESPONSIBLE PERSON
a. REPORT	b. ABSTRACT	c. THIS PAGE			Jeffery Owens
U	U	U	UU	57	19b. TELEPHONE NUMBER *(Include area code)*

Reset

Standard Form 298 (Rev. 8/98)
Prescribed by ANSI Std. Z39.18

TABLE OF CONTENTS

LIST OF FIGURES

LIST OF TABLES

1. SUMMARY

Current methods of decontaminating equipment contaminated by Chemical Warfare Agents (CWA) need significant improvement. To this end, the major objective of this work was to conduct research on development of effective nano and micro structured composite coatings capable to collect and decontaminate the chemical agents. In addition, the coating is intended to minimize the contamination cross-section of a coated vehicle. During the project we developed major components required to build effective protecting coatings against CWA. As a result of the work conducted several types of low-surface-energy coatings were created. Contact angles for water, hexadecane and warfare simulants (tributyl phosphate (TBP), methyl salicylate (MS) and 2-chloroethyl ethyl sulfide (CEES)) were determined for the coatings. The best coating demonstrated effective surface energy of 1.1 mN/m and contact angle with TBP of 128°. We also studied behavior of liquids on porous substrates as a model for micro- and nano-porous protective coatings. Currently there are several theories that aim to explain interactions of liquids with materials having micrometer-scale pores. However, it remains uncertain that these theories are applicable to materials with nanometer-scale pores. We have run a series of experiments on a well-defined model of protective layers on an alumina membrane to clarify this question.

2. INTRODUCTION

While soldiers would prefer military assets to not require any decontamination after exposure to Chemical and Biological Warfare Agents (CBWA), a self-decontaminating system as opposed to a coating, the reality is that this is not currently possible due to the number and complexity of the materials (glass, rubber, paint, metal, wiring, etc.) that comprise a typical military asset, coupled with the reality of field grime (mud, crud, blood, etc.). However, it is conceivable to: 1) considerably reduce the threat cross section associated with a contaminated vehicle, 2) decrease the logistics burden associated with decontamination, and 3) dramatically increase warfighter effectiveness when in a "required to fight/operate dirty (in a contaminated)" posture. Typically >70% of the exposed, contaminable surface area of a military asset is painted (>95% for airframes). Consequently, these advantages can be realized by modifying vehicle coatings to be self-detoxifying and easy to clean. Further, these modifications can be realized without sacrificing coating durability or signature.

The major objective of this work was to conduct research on development of effective nano and micro structured composite coatings with prescribed functional morphologies that allow for repellency of bulk CWAs and detoxification of minute absorbed amounts of CWAs. The coatings should be engineered on the nano or micro level. They should carry surface-energy-modifying groups. These groups, together with functional inclusions, are supposed to act against CWAs. The designed coating should be able to collect and decontaminate them. Simultaneously it should minimize the contamination cross section of a coated vehicle. During the project we developed major components required to build effective protecting coatings against CWAs. Specifically, two major components were developed. The first component is a low-surface-energy (LSE) coating with surface energy below 14 mN/m. The coating is based on thin polymer films filled with metal-oxide nanoparticles. The LSE is provided by incorporated fluorine-containing compounds. The coating demonstrates a low wettability by TBP utilized as a CWA model. The second component of the protective coating is able to arrest CWA droplets. Specifically, during the project we developed a polyacrylate-based coating able to swell with TBP utilized as a CWA model.

For the experiments on spreading of liquids on porous substrates we selected an alumina membrane as a model. Alumina membranes do not swell, their pore size distribution is narrow, and the pores are typically weakly, if at all, connected. Therefore, we can separate spreading and wicking effects from the effects of polymer swelling/absorption. We examined the classical Tanner law for drop spreading kinetics. Tanner's law describes drop spreading over smooth solid surfaces in terms of the change of the drop base radius, R, as a function of time, t, $R(t) \sim t^{1/10}$. The first set of experiments was focused on determining the kinetics of drop spreading on membranes with pore openings of different sizes. The second set of experiments was intended to examine the effect of fluid viscosity on droplet kinetics. TBP, diethyl phthalate (DEP), and hexadecane were chosen as simulants of different CWAs. We found that spreading on the membranes with conical pores having a small taper follows the Tanner law. On membranes with large taper we observed $t^{1/2}$ kinetics. We found that the square-root-of-time kinetics is associated with the formation of terraces governing the spreading kinetics. Raman micro-analysis and scanning electron microscopy (SEM) were used to study terrace formations. We also found that the spreading law drastically depends on the liquid viscosity: hexadecane and TBP have similar kinetics but DEP, which is about two times more viscous, always followed Tanner's law.

3. METHODS, ASSUMPTIONS, AND PROCEDURES

Within the scope of the project a series of LSE coatings were designed and tested. The coatings were made based on either i) commercially available polyurethane (PU) MIL-PRF-85285D, PU resin RW-7006-83A and activator RW-7006-83B, or ii) chemically modified poly(glycidyl methacrylate) (PGMA).

Al coupons and Si wafers were used as substrates. Al coupons were rinsed with acetone before the deposition of coatings. Highly polished single-crystal silicon wafers of [100] orientation (Semiconductor Processing Co) were used as a model substrate. The wafers were first cleaned in an ultrasonic bath for 30 minutes, placed in a hot piranha solution (3:1 concentrated sulfuric acid/ 30% hydrogen peroxide) for one hour, and then rinsed several times with high-purity water (18 MΩ–cm, Nanopure).

To obtain PGMA, glycidyl methacrylate (Aldrich) was polymerized radically (according to a procedure published elsewhere[1]) to give PGMA, $M_n = 300,000$ kDa, PDI = 2. The polymerization was carried out in methyl ethyl ketone (MEK, VWR) at 45 °C. 2,2'-Azobis(isobutyronitrile) (Aldrich) was used as an initiator. The polymer so obtained was purified by multiple precipitations from MEK solution in diethyl ether. To obtain PGMA films PGMA was dissolved in MEK at different concentrations and thin films were deposited on the substrate by dip coating and dried overnight. A dip-coater from Mayer Feintechnik, model D-3400, was used for the PGMA deposition.

The coatings were deposited on transparent poly(ethylene terephthalate) films or Al coupons using the adjustable micrometer film applicator "MICROM II" ("doctor blade" from Gardco, Paul N. Gardner Company, Inc., Pompano Beach, FL). A 1-to-1 ratio of base to activator was used. Nanoparticles were added to the resin to increase surface roughness. In this report, the amount of nanoparticles added to the coatings is described when a particular coating is discussed. The "doctor blade" was set to produce a "wet" film with the thickness of 20 mils (500 µm). The resulting thickness for the cured "dry" film varied from 10 to 12 mils (250–290 µm).

Thickness of the coatings on the model Si wafer surfaces was determined by ellipsometry. Ellipsometry was performed with a COMPEL automatic ellipsometer (InOmTech, Inc.) at an angle of incidence of 70°. Original silicon wafers from the same batch and silicon wafers with coating layer were tested independently and used as reference samples for the analysis of grafted polymer layers.

Morphology and roughness of the samples were tested by scanning probe microscopy (SPM) and performed on a Dimension 3100 (Digital Instruments, Inc.) microscope. We used the tapping mode to study the surface morphology of the films in ambient air. Silicon tips with spring constants of 50 N/m (tapping mode) were used. Imaging was done at scan rates in the range of 1–2 Hz. Root mean square (RMS) roughness of samples was evaluated from SPM images recorded. RMS roughness is the standard deviation of feature height (Z) values within a given area:

$$\text{Roughness} = \sqrt{\frac{\sum_{i=1}^{N}(Z_i - Z_{\text{ave}})^2}{N}} \tag{1}$$

where Z_{ave} is the average Z value within the given area, Z_i is the current Z value, and N is the number of points within a given area.

Contact angle (CA) measurements were performed with three liquids for wettability experiments: water, *n*-hexadecane and TBP. Water was chosen as a standard polar solvent for surface free energy calculations, hexadecane was chosen as a nonpolar hydrocarbon for surface free energy calculations, TBP was chosen as the CWA simulant.

To control the degree of surface modification, after each modification the CAs that the test liquids formed with the coatings were measured. The measurements were conducted at room temperature using a sessile drop method; equilibrating time was 60 sec. Results were recorded on the Drop Shape Analysis instrument (DSA, Kruss, Germany) with the DSA software. Based on the CA measurements, the surface free energies of all coatings and spreading coefficients of hexadecane and water on the coatings were calculated. CAs on each sample were measured for at least three times, were applicable, and average values were reported and used for the surface energy calculations.

To calculate surface energies of the coatings, total free surface energy is assumed to be splittable. In other words, the surface free energy is the sum of the dispersive and polar components, and can be calculated by the following equation[2]:

$$\gamma_s = \gamma_s^d + \gamma_s^p \tag{2}$$

in which γ_s^d and γ_s^p are dispersive and polar components of the surface energy (γ_s). These components can be derived from the system of two equations with two unknowns. If the CA with the surface, θ, and the surface tension and polar and dispersive components of at least two liquids are known, we can write[2]:

$$1 + cos\,\theta \approx 2\left[\frac{(\gamma_s^d)^{\frac{1}{2}}*(\gamma_1^d)^{\frac{1}{2}}}{\gamma_1} + \frac{(\gamma_s^p)^{\frac{1}{2}}*(\gamma_1^p)^{\frac{1}{2}}}{\gamma_1}\right] \tag{3}$$

$$1 + cos\,\theta \approx 2\left[\frac{(\gamma_s^d)^{\frac{1}{2}}*(\gamma_2^d)^{\frac{1}{2}}}{\gamma_2} + \frac{(\gamma_s^p)^{\frac{1}{2}}*(\gamma_2^p)^{\frac{1}{2}}}{\gamma_2}\right] \tag{4}$$

where $\gamma_1^d, \gamma_2^d, \gamma_1^p, \gamma_2^p$, are dispersive and polar components of two different liquids (1) and (2), respectively.

The droplet spreading on the alumina membranes was recorded with different high-resolution cameras placed on the Olympus MVX10 upright microscope. Pictures were taken from the top. To illuminate the whole object evenly and to make a clear image, relatively dim and diffuse

4

backlighting was applied: the light was located beneath the droplet, illuminating the whole object and allowing the terraces to be distinguished from the hemispherical cap. The drop diameter and volume were calculated from these pictures using the pixel-to-distance calibration.

The droplets were placed on Anodisc 25 membranes (Whatman$^{@}$) with a small (25.4-µm) wire, Figure 1. In each experiment, we took the picture of the drop as it was about to be deposited, and used this picture to estimate the drop volume by fitting its shape with Carroll's unduloid[3]. The membranes were secured in a Petri dish and held off the bottom of the dish by Scotch Brand double-sided sticky tape and also held in place by the tape as shown in Figure 2.
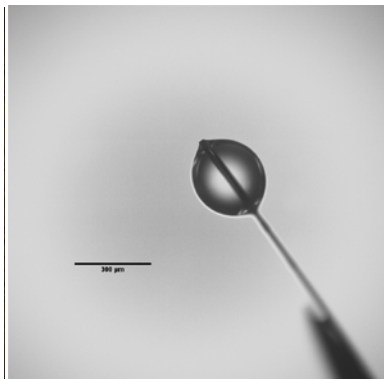
Figure 1. Droplet on the Wire
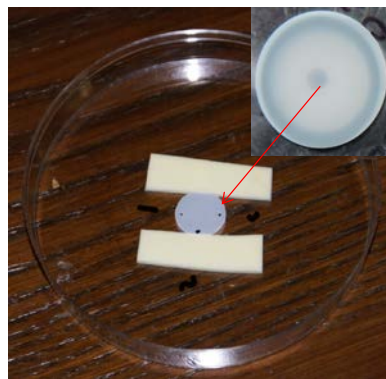
Figure 2. Set up of Membrane in Petri Dish

In Raman micro-analysis, a Bruker Optics SENTERRA dispersive Raman microscope was used with 785-nm laser, 20X and 50X bright field objectives, and 50x1000-µm aperture. We used a 10-sec integration time. The SEM images were taken with a Hitachi S-3700N ultra large chamber SEM with variable pressure and a Deben cold stage.

Four droplets of TBP and DEP were placed on two membranes with 39- and 95-nm pore diameters, and three droplets of TBP and DEP were placed on two membranes with 164-nm pore diameter. Each drop was secured in a closed Petri dish, which was opened only when the measurements were performed. The pictures of each droplet were taken after being placed, a few minutes after, 30 minutes after, 15 hours, 24 hours, 48 hours, 72 hours, 96 hours, 120 hours, 144 hours, 1 week, 2 weeks, 3 weeks, and 4 weeks after.

4. RESULTS AND DISCUSSIONS

4.1. Model Coatings

Model coatings based on commercially available polyurethane MIL-PRF-85285D and PU resin
RW-7006-83A and activator RW-7006-83B were prepared according to the following recipes:
> MIL1 and MIL2 : Coatings from commercially available polyurethane MIL-PRF-85285D
> without (MIL1) and with (MIL2) added titanium dioxide particles;
> RW1 and RW2: coatings from RW-7006-83A and one part of activator RW-7006-83B
> without (RW1) and with (RW2) added one part by mass titanium dioxide particles.
> Ti-1–Ti-4: layers from titanium dioxide particles on glass slides.

After preparation the coatings were modified with 1H,1H,2H,2H-perfluorodecyltrimethoxysilane
(PTS) to decrease the coating's surface energy. CA with water and hexadecane were measured
and surface energies were calculated. For calculations of surface energy CAs of water and of
hexadecane were used.

Measured CAs and calculated surface energies for the coatings are presented in Table 1 and
Figure 3, respectively.

Table 1. Contact Angles of Surfaces Prepared with and without Titanium Dioxide Particles

Sample ID	Method of preparation		Nanoparticles		Average CA	
	Base	Base–to-Activator Ratio	Name/ Material	Size, μm	Water	Hexadecane
MIL1	MIL-PRF-85285D	1 to 1	NONE	N/a	89.2	~ 18
MIL2	MIL-PRF-85285D	1 to 1	TiO_2 = 1 to 1 (to base by mass)	~ 0.5	86.7	~ 17
RW1	RW-7006-83A	1 to 1	NONE	N/a	98.8	~ 18
RW2	RW-7006-83A	1 to 1	TiO_2 = 1 to 1 (to base by mass)	~ 0.5	93	0

As an example, data for CA measurements of two liquids for the coating RW1 and values of
dispersive and polar components of the two liquids are presented in Table 2.

Table 2. Contact Angles of Liquids RW1 and Surface Tension Data for Two Liquids

Liquid	Contact angle, θ	$\gamma_{1,2}$, mN/m (literature value[2])	γ^d, mN/m (literature value)	γ^p, mN/m (literature value)
water	98.8	72.8	21.8	51
n-hexadecane	18	27.47	27.47	0

Following are the major conclusions made from preparation and evaluation of the model
samples:

1. Measured CAs with water of commercial (MIL) and Tyndall's (RW) coatings showed that these materials are hydrophobic; water CA 85°~100°. Exposed to organic liquids, these materials are oleophilic. CA with hexadecane is <20°;
2. RW coatings have larger CA with water than that of MIL-PRF-85285D. This is explained by the presence of fluoropolymer in the RW coating;
3. Addition of titanium dioxide particles to the coatings decreases the hydrophobicity and oleophobicity of coatings prepared from RW (Table 1) For example, the surface energy of coating changed from 26.8 mN/m for pure RW1, to 28.7 mN/m for RW2 after the addition of TiO_2 nanoparticles;
4. Treatment of the coatings (MIL and RW) with PTS decreases surface energy, thus increasing hydro/oleophobicity (Fig. 3).
5. Plasma etching of coatings with nanoparticles creates additional roughness on the surface and, following silane treatment of the rough surface, produces a hydrophobic/oleophobic surface with surface energy = 13 mN/m (sample RW2-3, Fig. 3), CA with hexadecane = 77 °.
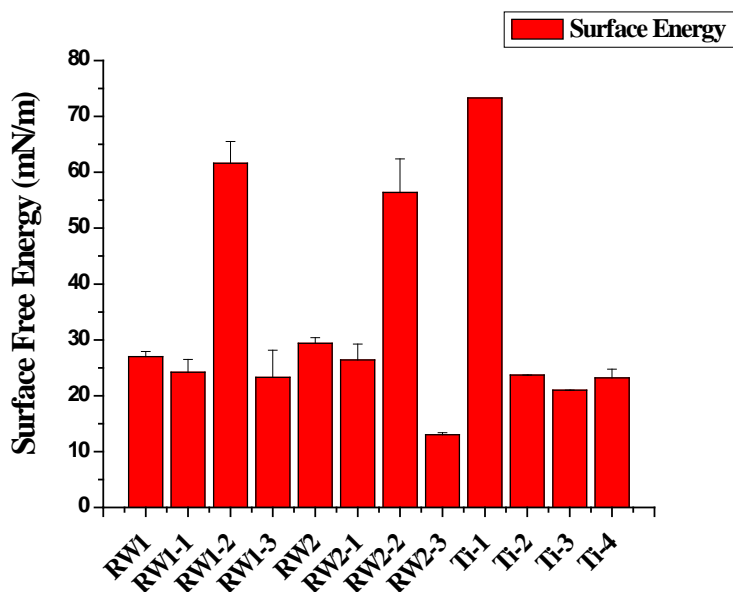
Figure 3. Surface Free Energy Calculated for Various Model Samples
*Sample identification for the surface treated samples: RW1-1 (silane-treated RW-1), RW1-2 (plasma-etched RW1), RW1-3 (silane-treated RW1-2), RW2-1 (silane-treated RW2), RW2-2 (plasma-etched RW2), RW2-3 (silane-treated RW2-2), Ti-1 (as-received TiO_2 on glass), Ti-2 (silane-treated TiO_2 on glass), Ti-3 (silane-treated TiO_2 on glass cured for 5 days), Ti-4 (silane-treated TiO_2 on glass cured at 120 °C for 2 h).

4.2.   Coatings with Increased Wt% Loading of Titanium Dioxide Particles

To increase surface roughness, coatings with different particle loadings were prepared. For experiments with different loadings, the RW polymer and TiO_2 nanoparticles (DuPont, spheres

300–500 nm in diameter) were used. Coatings with increased amount of nanoparticles were compared to the ones with the basic loading used in the previous experiments (in which TiO_2 was added at 1 to 1 to the base ratio). This base loading was recalculated into wt% of dry coating mixture (1 part base and 1 part of activator to 1 part of titanium dioxide particles by mass) and comprises 33 wt% of TiO_2. TiO_2 loading correspondingly was increased as follows: 43 wt% (1.5 to 1), 50 wt% (2 to 1), 60 wt% (3 to 1), 67 wt% (4 to 1), and 71 wt% (5 to 1). All sample coatings were treated with plasma and silane as previously reported and CAs before and after the treatment were measured. Then surface free energy was calculated based on CA for the coatings with water and hexadecane. Roughness of the samples due to addition of titanium dioxide particles was measured by atomic force microscopy (AFM). The surface free energy and contact angles were corrected using the Wenzel roughness factor, estimated by a standard[4] equation.

With increasing loading of titanium dioxide nanoparticles the roughness of the surfaces at nanometer scale increases. Also, with increasing titanium dioxide loading, the number of peaks per μm^2 and the real surface area increase. Roughness data for coatings before and after the plasma etching/silane treatment do not show significant difference in averaged surface free energy values.

Major conclusions on the influence of titania loading on the coating properties are presented below

1. Surface free energy does not change significantly with increased loading of titania nanoparticles. This observation suggests that the major contribution to the surface energy is from RW polymer present on the coating surface. After plasma etching/oxidizing and the silane treatment with PTS, surface free energy drastically decreases (Fig. 4).
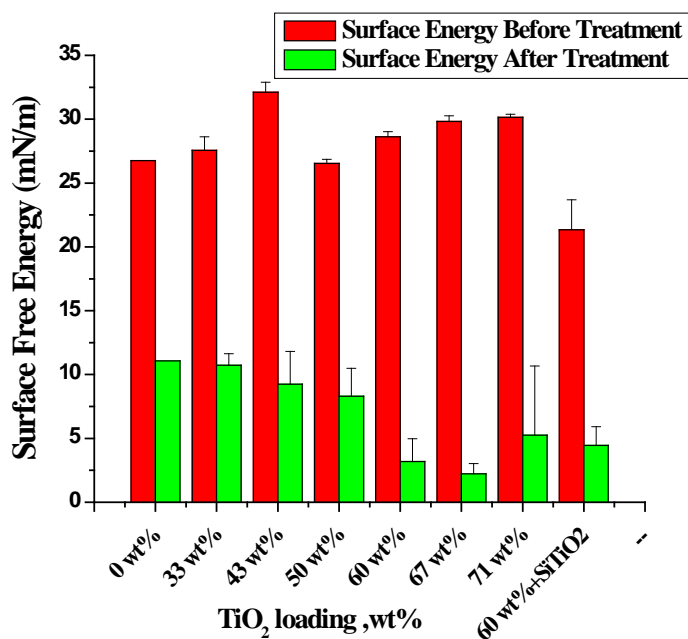
Figure 4. Surface Free Energy of Coatings vs. TiO_2 Nanoparticle Loading before and after the Plasma Etching/Silane Treatment

2. On rough surfaces observed CA (which from a practical standpoint is more important) is different from the true CA. Therefore, some corrections by r^W, the Wenzel roughness factor, should be made to find the true or equilibrium CA. We used the method suggested by Kamuzevitz and Possart[4], where $r^W = r^{AFM} = A_{image}/A_{geom(scan\ field)}$. The rougher the surface, the higher the r^{AFM} value. Corrected CAs and surface free energies calculated using the equilibrium CAs are presented in Figure 5.

3. The critical loading of TiO_2 nanoparticles, after which CAs do not increase, was around 67 wt% (Fig. 4). The CAs at 67 wt% loading after etching/silane treatment are $CA_W = 142°$, $CA_{Hex} = 116°$, apparent surface free energy $\gamma = 2.24$ mJ/m^2; corrected by Wenzel roughness, $CA_W = 116°$, $CA_{Hex} = 104°$, corrected apparent surface energy = 6.35 mJ/m^2.
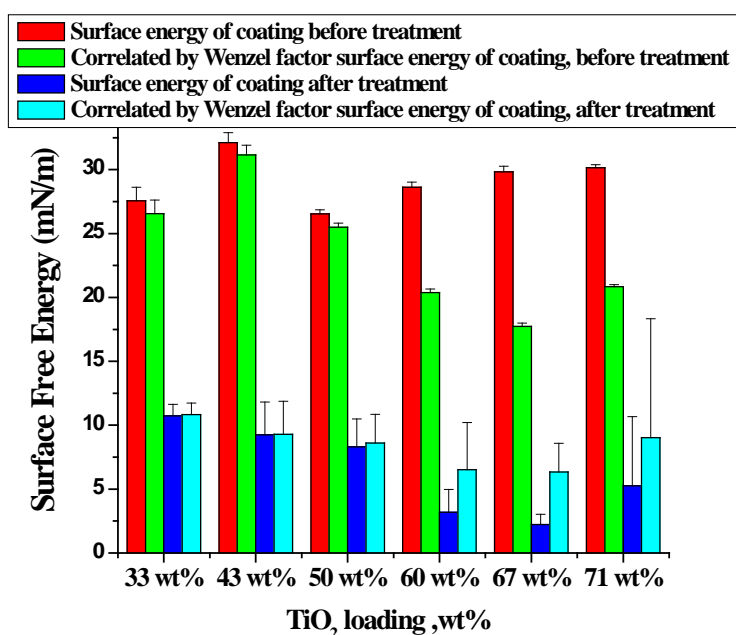
Figure 5. Combined Data for Surface Energy of Coatings before and after Plasma Etching/Silane Treatment, Apparent and Corrected by Wenzel Roughness Factor

4.3.   Liquid and Vapor Silane Treatment

Two different silane treatments were performed and compared. Specifically, vapor treatment was done for 48 h at room temperature, and liquid treatment at 105 °C for 1.5, 3 and 4.5 h of curing time. Experiments to compare vapor and liquid silane treatment did not show significant difference in the CAs. Since both liquid and vapor silanization give similar results the treatment method can be chosen solely based on economical and technological preferences.

4.4.   Coatings with Silanized Titanium Dioxide

The titanium dioxide nanoparticles were also treated with PTS from solution in 2-propanol. As a result of the treatment, silanized, hydrophobic TiO_2 nanoparticles were obtained. A non-treated

9

coating containing 67 wt% silanized TiO$_2$ (Si-TiO$_2$) shows a higher CA with hexadecane, ~ 43°, and the apparent surface free energy was calculated to be 20.84 mN/m. Conversely a coating containing 67 wt% plain TiO$_2$ shows zero CA with hexadecane (apparent surface energy calculated to be 29.75 mJ/m^2). CA for both coatings with water before treatment does not differ significantly, as well as CAs with water and hexadecane after plasma etching/silane treatment. However, we expect the coating with silanized particles to be more abrasion resistant. In fact, if by some physical force the thin top layer of the coating were to be destroyed, the body of coating may still be water- and oil-resistant due to the presence of the silanized nanoparticles.

4.5.   TBP Dynamic Contact Angles of the Coatings

CAs with TBP were measured on the PTS-treated coatings with basic loading of TiO$_2$ particles (33 wt%), a coating with the highest CAs with hexadecane and water (67 wt%) and a plain coating (0 wt% loading). An interesting behavior of the liquid on the coatings was observed. Namely, TBP CA was changing with time. For the 67% coating the change was from 52° to ~24° during 7 min (Fig. 6). Experiments on absorbance of TBP by pure RW coatings (no particles) showed that coating absorbs ≈ 1 wt% of applied TBP. From square-root-of-time dependence at the initial stage of spreading one may infer that spreading of TBP on the coating is facilitated by absorption and diffusion.
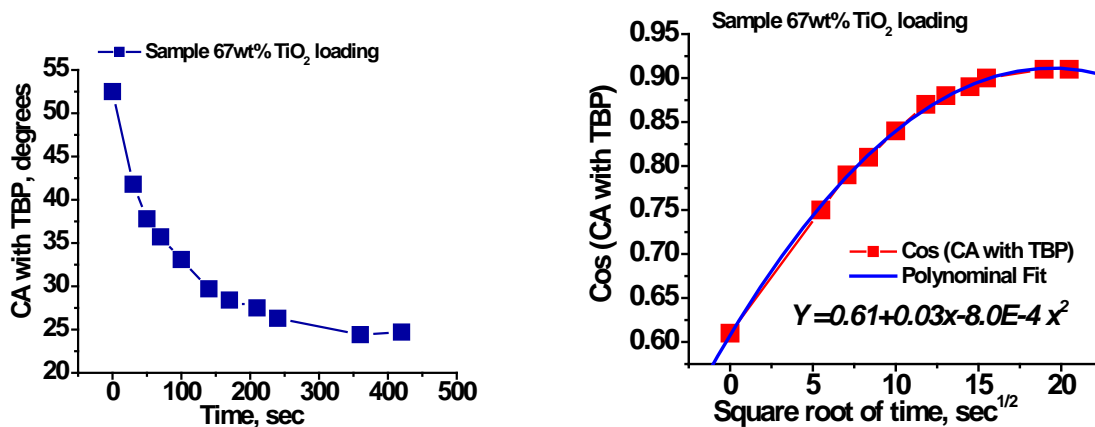
Figure 6. Graphs, Representing Change of TBP Contact Angle with Time on Surface Coating with 67 wt% TiO$_2$ Loading: (left) Exponential Decay of Apparent CA of TBP on Coatings Taken against Time in Seconds; (right) Cosine of the CA Drawn against Square Root of Time

To further investigate interaction of TBP with RW, TBP vapor absorption by coatings made of plain RW polymer was studied with ellipsometry. *In situ* ellipsometric study of absorption of TBP vapor showed continuous swelling of the plain RW coating. The thickness increased from approximately 90 nm to 130 nm during 4 days, indicating affinity of TBP to the RW coating.

CAs with CEES (Aldrich 98%, C$_4$H$_9$ClS), a sulfur mustard simulant, were measured on a coating with 67% loading of TiO$_2$ particles. The CA of 112 ± 1° was observed, (Fig. 7).

Surface energy was calculated without taking into account the Wenzel roughness factor
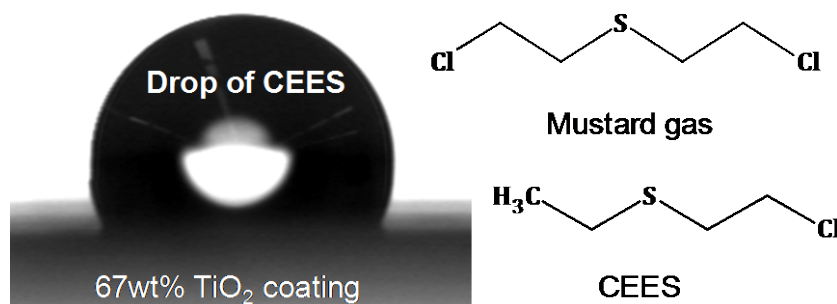
Figure 7. CEES Contact Angle (112 ± 1°) for Coating with 67 wt% TiO$_2$ Loading after Etching/Silane Treatment

4.6.   Coatings from Mixtures of Titanium Dioxide Particles and Alumina Whiskers

To investigate the influence of inorganic fillers on coating performance, coatings were prepared with 0.5 and 1 parts of alumina whiskers to 1 part of titania nanoparticles. AFM images of coatings prepared from these mixtures show exposed smaller nanoparticles tht appeared to be rather spherical. We do not observe the presence of elongated nanoparticles as we would expect from nanowhiskers (Fig. 8).
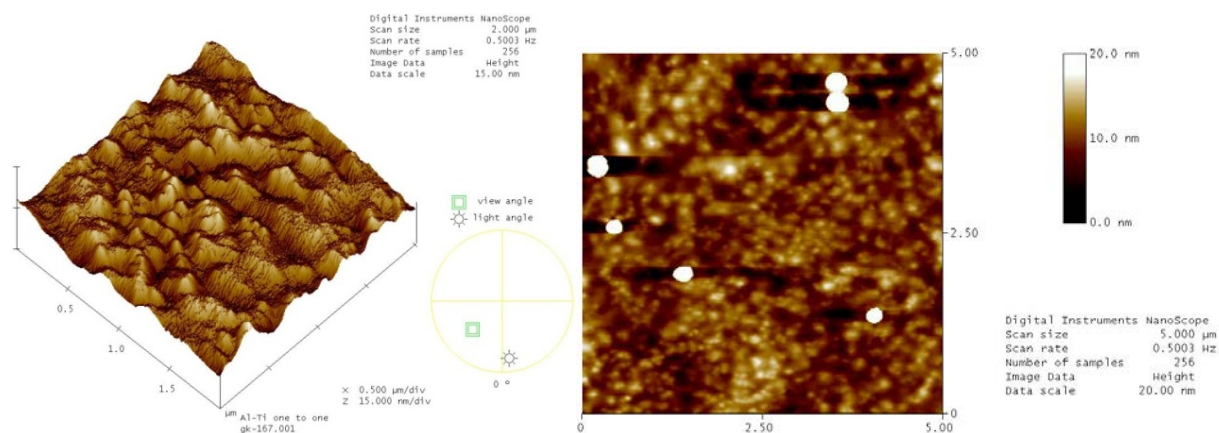
Figure 8. AFM Images of Coating Prepared with mixture of Alumina Whiskers and Titanium Dioxide Particles in 1 to 1 Ratio by Mass: (left) Image Surface Plot, Scan Sixe is 2 x 2 μm^2; (right) Topographical Image of the Same Coating with Scan Size of 5 x 5 μm^2

A likely reason for the absence of the whisker-like particles is that the whiskers were broken during coating preparation, which includes sonication and stirring with small alumina beads. Moreover, coatings prepared from the mixture of aluminum oxide nanowhiskers and titanium dioxide nanoparticles did not show the difference in CAs from the basic coatings.

4.7.   Coatings of Plain RW Polymer (From Tyndall), RW Polymer with 33 wt% and 67 wt% TiO$_2$ Loading on Aluminum Coupons for Testing with Real Chemical Agents

For the study of interaction of the coatings with real CWAs, TiO$_2$ coatings on aluminum coupons were prepared and sent to Tyndall AFB. CAs with water and hexadecane were measured for these samples to compare with the results previously obtained. CAs with MS, which was used as a mustard simulant, were measured as well.

In general, CAs for the coatings on aluminum coupons showed the same trend as those in the experiments previously reported. Before the surface treatment, hexadecane on 67 wt% TiO$_2$ RW coatings spreads completely, while on 0 wt% coatings it forms an angle of ~ 14° and on 33 wt% coatings it forms angle of ~10°, Figure 9(a). This behavior was explained previously by the increased loading of TiO$_2$ nanoparticles possessing higher surface energy. Overall, CAs measured for new samples prepared on aluminum coupons show slightly smaller values, Figure 9. The possible reason for the smaller CAs may be the environmental conditions at which silanization or/and CA measurements were made (23–24% humidity). Another reason could be in the substrate used for the new coatings. Previously as a substrate poly(ethylene terephthalate) films were used, which slightly bent to reduce stress induced by drying of the coating. The new rigid substrate, aluminum coupons, keeps its dimensions, and therefore the coating layer should accommodate stress from the drying.

CAs for MS were determined to be lower than the angles for CEES. CA for CEES was ~ 112°, and on the similar surface CA for MS was ~ 53°.

4.8.   Coating Modification with Longer Perfluorocarbon Chains Compounds

The majority of the fluorine-containing coatings utilized in this project initially were modified via silanization with PTS, which contains eight carbon atoms with fluorine attached to them. To test the influence of length and branching in the perfluorocarbon tail, silanes with longer chains were used for surface treatment. Specifically, a mixture of perfluorododecyl-1H,1H,2H,2H–triethoxysilane and perfluorotetradecyl-1H,1H,2H,2H-triethoxysilane (**PD-TDES, Gelest Inc)** was used for the silanization. Silanization was done from liquid and vapor phases at 85 °C overnight, and then the sample was rinsed with MEK. After the treatments, CAs with water, TBP and hexadecane were measured and compared.

CAs of water on treated surfaces showed the same trends as with PTS, being in the range of 125 to 130°. However, TBP and hexadecane showed inconsistent values of CA after these silane treatments. CA with hexadecane and TBP were determined to be 98.5° and 17.5°, respectively, after the PTS treatment. In contrast, for the PD-TDES-treated surface we observed wetting with hexadecane and TBP after the treatment. We hypothesize that during treatment we did not obtain a robust, cross-linked silane layer, which led to inconsistent results in the CA measurements. Surface energies of treated surfaces were estimated based on the water and hexadecane CAs. The results indicated that the surface energy of the PD-TDES-treated surface was 30.6 mN/m, which is higher than that of the PTS-treated surface (5.2 mN/m).

To investigate the influence of branching on coating surface energy, linear perfluorododecanoic acid (PFDOA) (from Acros Organics) and branched perfluoro-3,5,5-trimethylhexanoic acid (PFTMHA) (from SynQuest) were used for modification of a model surface, an Si wafer. Before perfluoroacid modification, Si wafers were dip coated with PGMA and annealed at 110 °C. After a rinse with MEK to remove any unbonded polymer, vapor deposition of PFDOA or PFTMHA

was performed at 120 °C for 3h. Finally, samples were rinsed with MEK four times to remove any unattached molecules. CAs of TBP, hexadecane and water were measured three times and
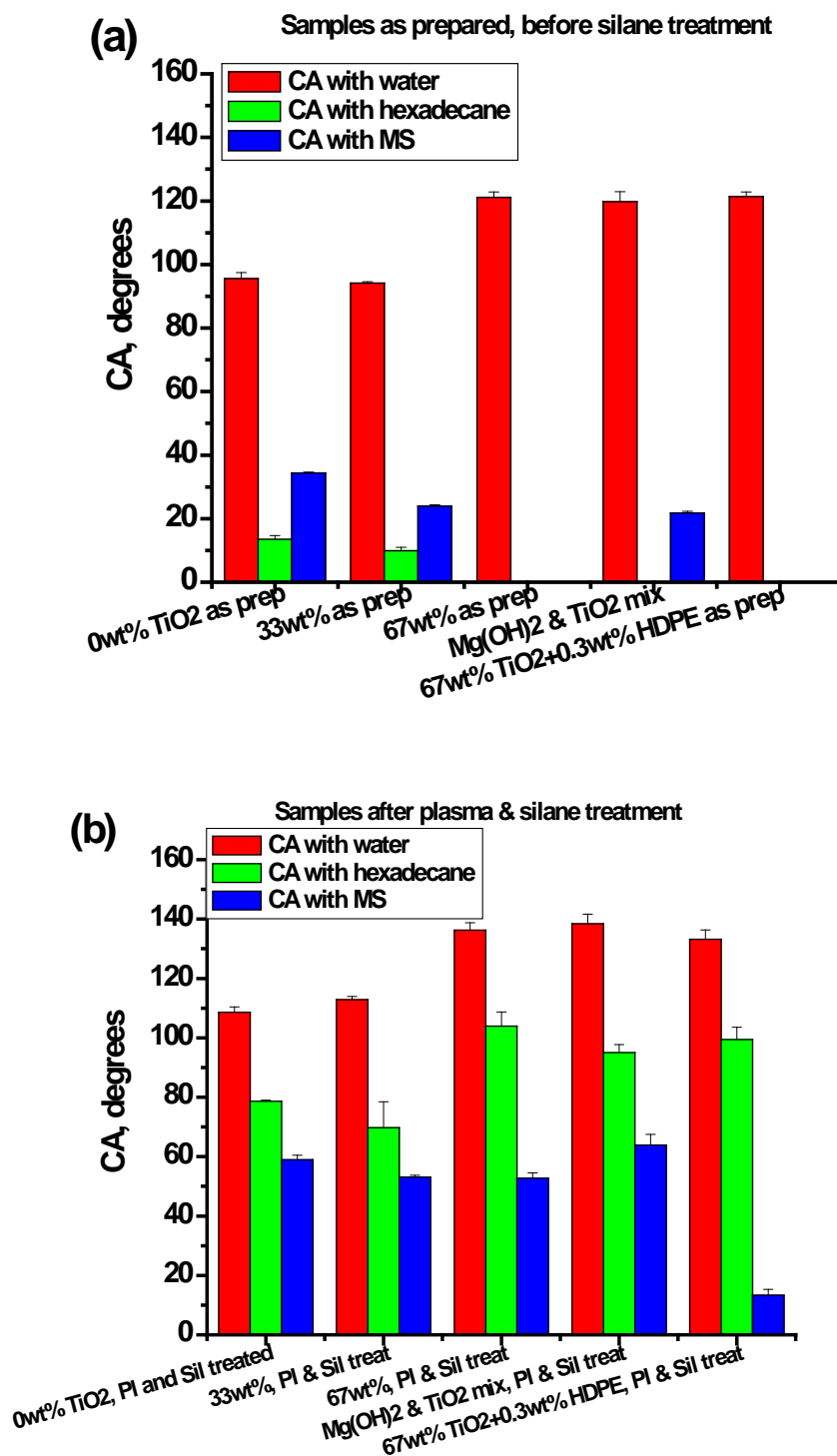
Figure 9. Contact Angles on Surfaces before (a) and after (b) Plasma Etching and Silane Treatment

The absence of green and blue bars next to the red bars in (a) indicates that the hexadecane and/or MS immediately absorbed into that sample.

their averages are shown in Figure 10. Based on the CA results, PFTMHA makes surfaces less hydrophobic than does PFDOA. In addition, CAs of TBP and hexadecane are lower for PFTMHA-treated surfaces. Surface energies of treated substrates were calculated using hexadecane and water CAs. The results indicate that the surface energy of the PFTMHA-treated surface was 26.2 mN/m, which is higher than the energy of the PFDOA-treated surface, calculated to be 12.7 mN/m (Fig. 10). It is necessary to point out that PFDOA-treated surfaces demonstrated a relatively high CA (69°) for TBP, significantly higher than the one for PTS (17.5°) previously employed. This positive result led us to a decision to use PFDOA treatment in most of our next experiments.
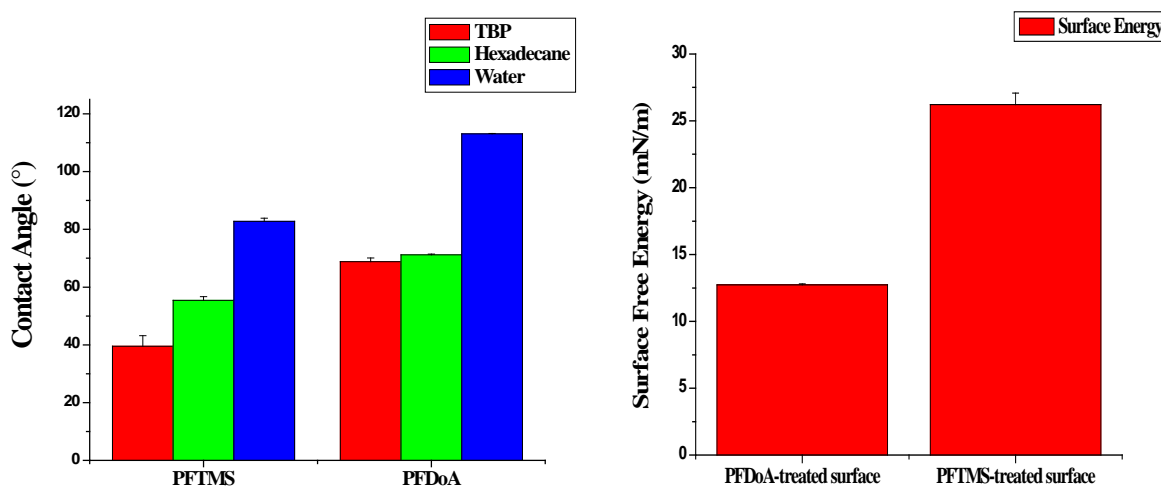
Figure 10. CA of Water, TBP and Hexadecane on PFDOA- and PFTMHA-Treated Surfaces and Respective Surface Energies

4.9. Modeling of Decontamination Patches on Low-Surface-Energy Coating

Decontamination patches should swell well with TBP and hexadecane. Therefore, swelling capability of different polar or non-polar polymers with TBP was determined. Eventually, a polyacrylic acid copolymer with poly(oligoethylene glycol methacrylate) (PAA-POEGMA) and PGMA was chosen for the creation of patches on the surface of the coatings.

In preparation of the patches for TBP, the challenge was to attach patches to the LSE fluorinated coating. For this purpose, we prepared 5:1, 10:1 and 20:1 mixtures of PAA-POEGMA and PGMA-POEGMA copolymers to increase patch adhesion to the surface. The mixture was applied manually to the surface to obtain the patches. After the deposition samples were annealed at 110 °C for 3h and rinsed with MEK, CA on the patches was measured. CAs of water, TBP and hexadecane on patches were measured and compared with CAs on treated surfaces (Fig. 11).
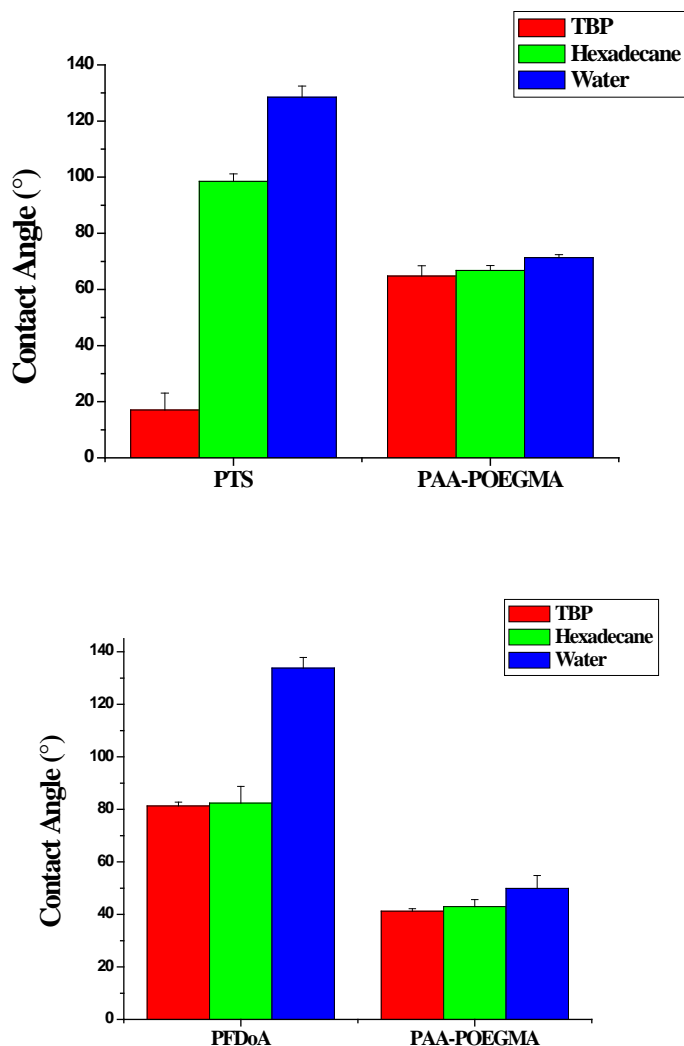
Figure 11. CA with Water, TBP and Hexadecane on Silane (PTS)- and Perfluorododecanoic Acid (PFDOA)-Treated Surface and 5:1 PAA-POEGMA-PGMA-POEGMA Patches

CAs with solvents on patches is lower than on the treated surfaces. However, the nature of any pretreatment of the surface (with PTS or PFDOA) influences CA on patches. Namely, CAs on patches after PTS treatment were higher than after PFDOA treatment. Surface energy of the patches was estimated. It was found that surface energy of patches on PFDOA-treated coatings was significantly higher than that of those on PTS-treated coatings.

PAA-POEGMA-PGMA-POEGMA patch swelling with TBP was tested. Preliminary results in Figure 12 show that TBP is absorbed by patch material, but relatively slowly.
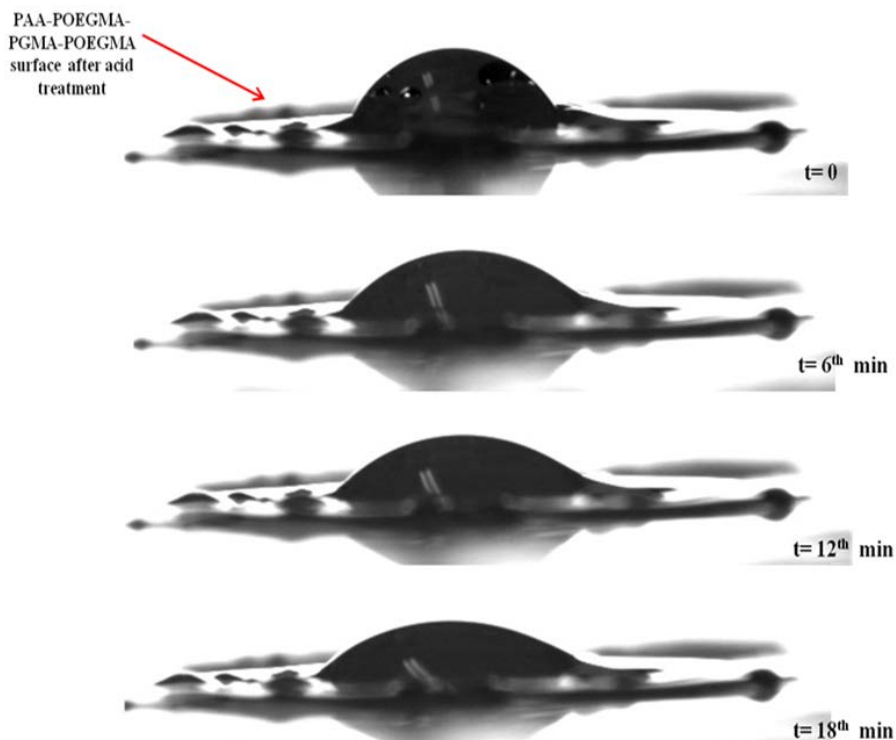
Figure 12. PAA-POEGMA-PGMA-POEGMA Patch Swelling with TBP

PGMA patches were deposited on a PTS-modified surface. An array of the patches was tested for arresting a rolling droplet of hexadecane. Static CAs with hexadecane on PGMA patches on PTS-treated coatings were found to be ~ 72.3° and on the PTS-treated coatings itself ~ 90.1°. Snapshots of hexadecane droplet movement on PGMA patches are shown in Figures 13 and 14.
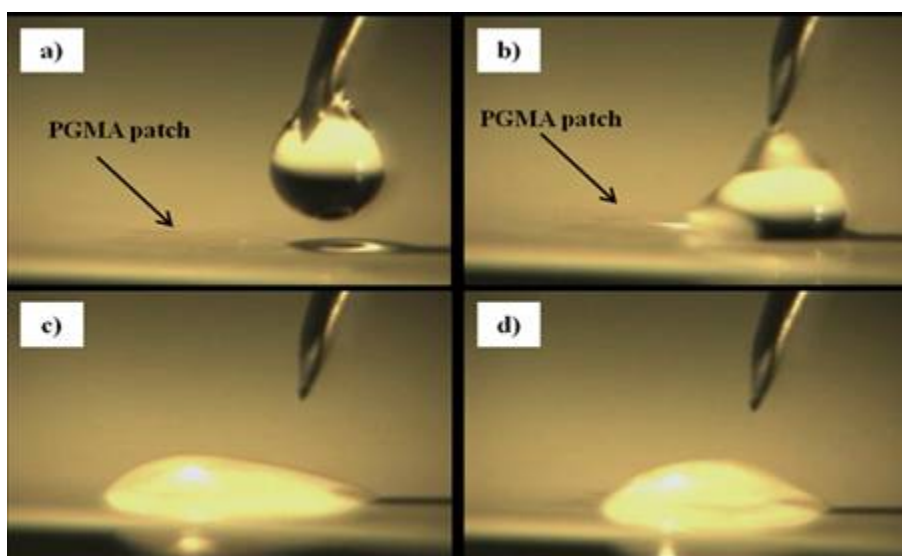
Figure 13. Movement (Arresting) of Hexadecane on PGMA Patched Surface: (a, b) Hexadecane Dropped near the PGMA Edge; (c, d) Hexadecane Droplet Moves through the PGMA Patch
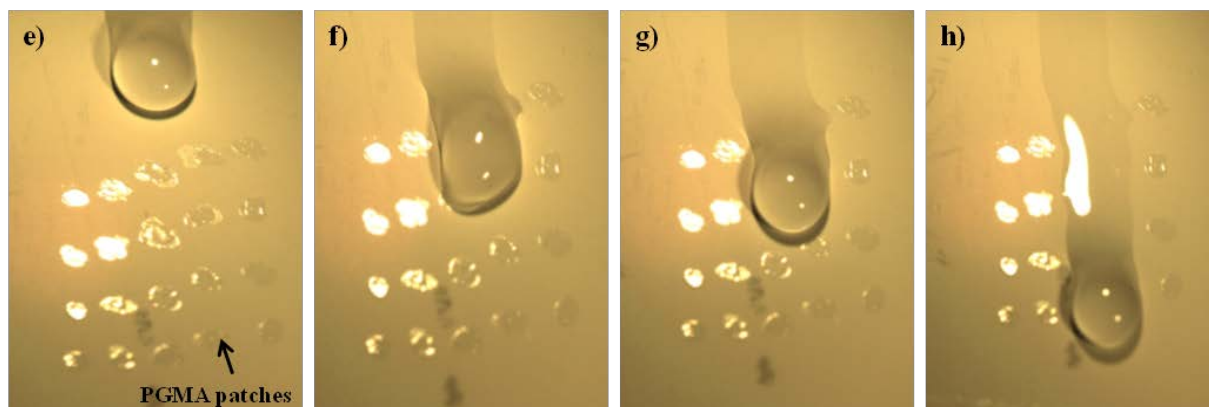
Figure 14. Hexadecane Moves through PGMA Patches on the Tilted (~45°) Surface and Stops

4.10. Low-Surface-Energy Coatings on Rough Surfaces

Due to the fact that PFDOA-treated surfaces exhibit the highest CA with TBP, a set of rough surfaces were modified with PFDOA and their characteristic were investigated. Specifically silicon wafer, nickel, aluminum coupons, alumina membranes, and filter paper were modified with PFDOA. For modification, most of substrates were plasma treated for 20 min; filter paper was treated for 5 min. Then they were rinsed with water, dried, coated with PGMA and annealed at 110 °C for an hour. After rinsing with MEK, vapor deposition of PFDOA on substrates was performed at 120 °C for 3 h with subsequent rinsing with MEK four times to remove any unattached molecules. CAs and corresponding surface energies for each substrate are presented in Figures 15 and 16. Alumina membrane has shown the highest CA with TBP, most likely due to its highly porous structure.

4.11. Solution Grafting of Perfluorododecanoic Acid (PFDOA) and Perfluorohexanoic (PFHXA) Acid

We have compared hydrophobic and oleophobic properties of the perfluoro carboxylic acids with various perfluoroalkyl chain lengths. Specifically, solution grafting of perfluorocarboxylic acids such as PFDOA and perfluorohexanoic acid (PFHXA) (from SynQuest) was conducted. 0.02M and 0.03M solutions of acids in MEK were used for modification of model Si wafer surfaces. Before perfluorocarboxylic acid modification, Si wafers were dip coated with PGMA and annealed at 110 °C. After rinsing with MEK to remove any unbonded polymer, Si wafers were immersed in acid solutions at 65°C and grafted for different times. Finally, samples were rinsed with MEK four times to remove any unattached molecules. CAs of TBP and water were measured (Fig.17). From Figure 17, it can be seen that the PFDOA modification is more effective than PFHXA modifications to obtain hydrophobic/oleophobic surface. It was found that there was a significant difference between the CA of TBP on PFHXA-treated surface and PFDOA-treated surface. CAs with TBP on PFDOA-treated surfaces, which were prepared using 0.02M and 0.03M PFDOA–MEK solutions, are almost independent of acid concentration used for grafting.
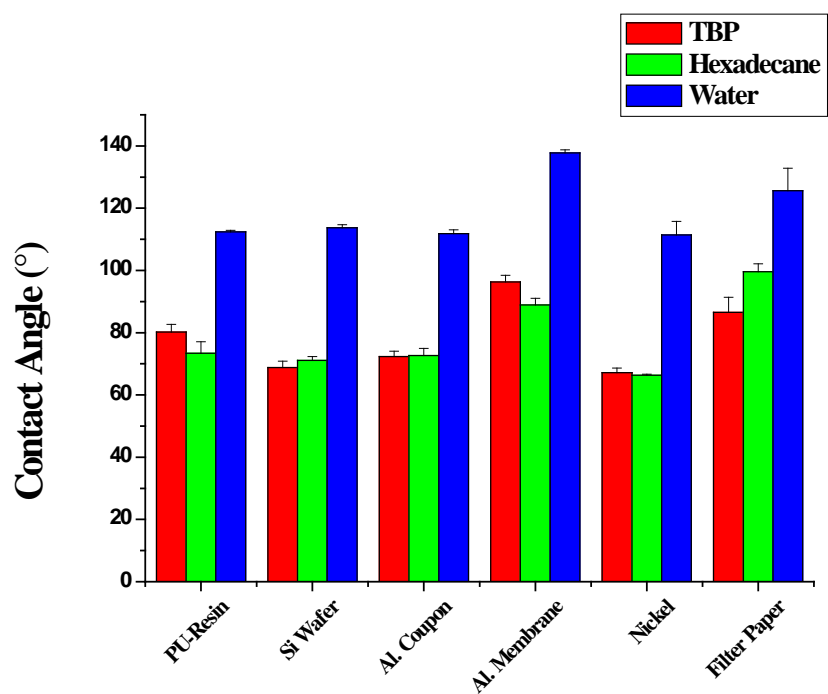
Figure 15. CA of TBP, Hexadecane and Water on PFDOA-Treated Substrates
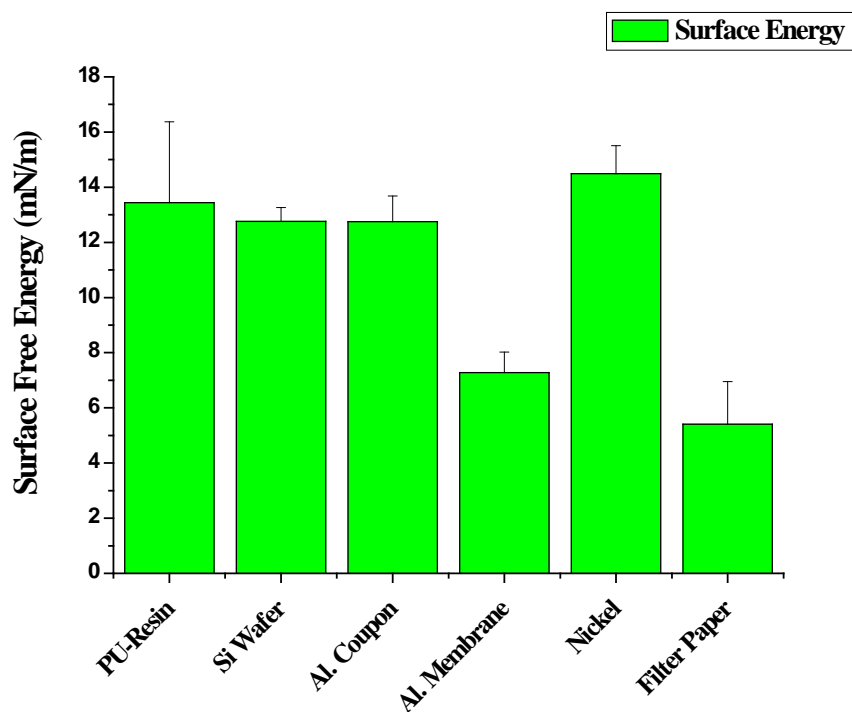
Figure 16. Surface Energy of PFDOA-Treated Surfaces
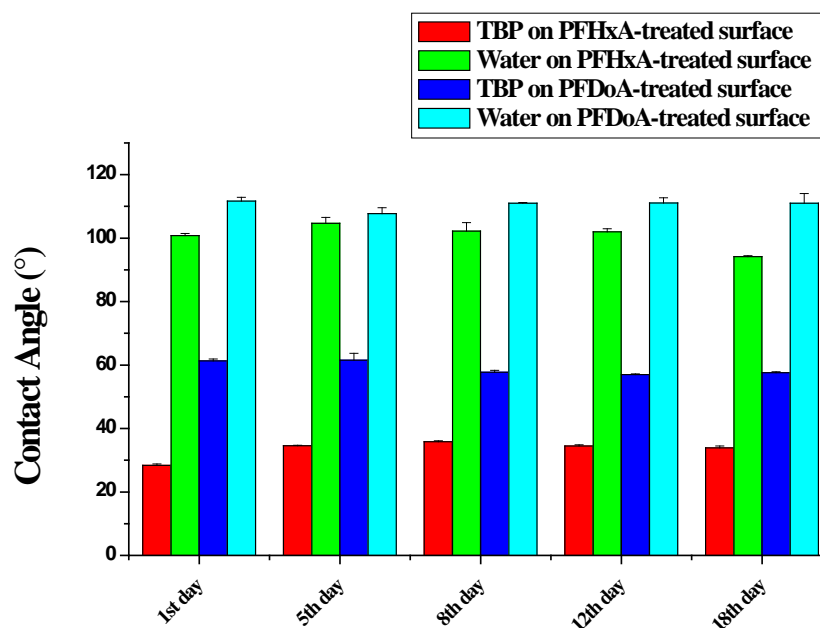
Figure 17. Contact Angles of TBP and Water on Surfaces Treated with PFDOA and PFHXA Solution (0.02M)

4.12. Modification of the Titanium Oxide Particles with PFDOA

Titanium oxide particles were modified with PFDOA using either solution treatment or vapor treatment. For solution treatment, PGMA-coated TiO_2 particles were treated using 0.03M PFDOA solution in MEK at 65 °C for 5 days. After removal of unbonded acid, the TiO_2 solution was drop cast on the different surfaces. CAs of TBP, water and hexadecane were measured. For the vapor treatment, PGMA-coated TiO_2 particles were mixed with PFDOA and treated under vacuum at 120 °C overnight. Solution-treated TiO_2 particles were drop cast onto four surfaces: Si wafers and PU-resin surfaces untreated and the same after treatment with PFDOA. CAs of TBP, hexadecane and water on these surfaces were measured and shown in Table 3. CA data indicated that all surfaces were superhydrophobic; however, CAs of hexadecane on all of the surfaces tested did not exceed 53°. Moreover, TBP placed on the surfaces penetrates the coatings with time.

Table 3. CAs of TBP, Hexadecane and Water on Different Treated Surfaces*

Penetrant	Contact Angle (Degrees) for TiO$_2$-PFDOA on			
	Si Wafer			PU Resin
		PGMA Coated	PFDOA Treated	PFDOA Treated
TBP	*penetrates fast*	*penetrates fast*	*penetrates slowly*	*penetrates slowly*
Hexadecane	52.4	43.8	46.4	53
Water	142.4	143.6	142	141.2

* Only one contact angle measurement was done for each surface

TiO$_2$ particles were modified using vapor treatment with PFDOA. Modified particles were used for preparation of PU-resin coating. In the parallel experiment PU resin filled with untreated titania particles was prepared. Wettability of both surfaces was compared. It was found that CA of water on the PU-resin coating made with untreated TiO$_2$ particles was higher than on the resin surface made with PFDOA-treated TiO$_2$ particles. We attribute this fact to poor miscibility/dispersivity of PFDOA-treated particles with base of PU resin.

4.13. Grafting Perfluorocarboxylic Acids to PGMA Layers of Different Thickness

Model silicon wafer surfaces coated with PGMA layers of different thicknesses were modified with PFDOA or PFHXA. Acid grafting was done from the vapor phase at 120 °C. The effect of PGMA annealing temperature on perfluorocarboxylic acid grafting was also investigated. Specifically, Si wafers dip coated in 0.5% PGMA solution were annealed at 50, 70 and 90 °C. Then they were grafted with either PFDOA or PFHXA at 120 °C overnight. In addition, non-annealed PGMA-coated Si wafers were grafted with PFDOA or PFHXA. CAs of TBP, hexa-decane and water were measured and the surface energies of modified Si wafers were calculated.

The effects of PGMA thickness on PFDOA and PFHXA grafting and wettability were investigated. Different PGMA thicknesses were obtained by dip-coating surfaces in PGMA solutions of different concentrations. After crosslinking with PGMA at 110 °C for an hour, surfaces were grafted with perfluoroacids. Increasing the PGMA thickness caused no significant differences in CA measurements after PFDOA treatment (Fig. 18). The effects of PGMA thickness on PFHXA treatments are shown in Figure 19. It was found that CAs of hexadecane increased from 53° to 64° as PGMA thickness was increased from 2.3 nm to 35.2 nm; however, no significant change in CAs of either water or TBP was observed. From CA measurements it was found that the surface energies of PFHXA-treated surfaces were close to each other and independent of PGMA thickness. The surface energy of PFDOA-treated surfaces was lower than that of those treated with PFHXA.
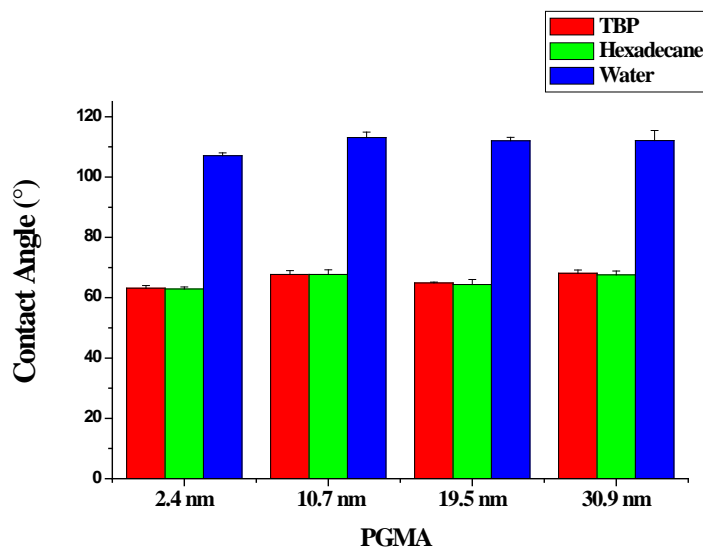
Figure 18. Contact Angles of TBP (■), Hexadecane (■) and Water (■) on PFDOA-Treated Silicon Wafers with Different PGMA Thickness

21
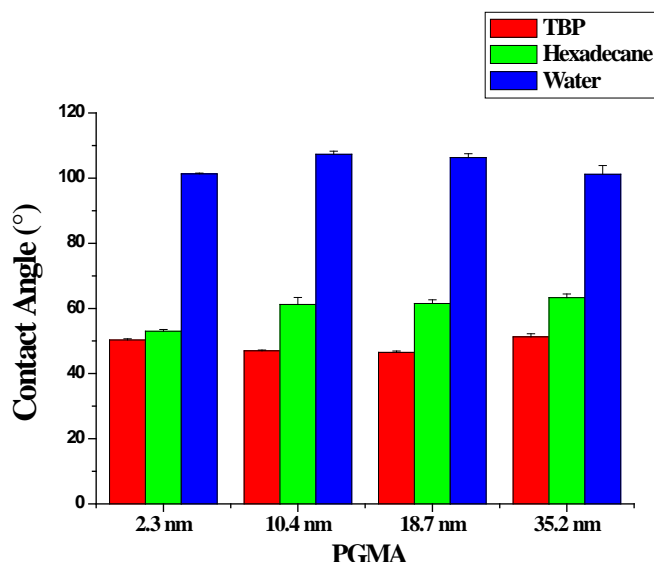
Figure 19. Contact Angles of TBP ( ), Hexadecane ( ) and Water ( ) on PFHXA-Treated Silicon Wafers with Different PGMA Thickness

Effects of the PGMA annealing temperature on perfluorocarboxylic acid grafting were investigated. There was no significant change in sample wettability for different PGMA annealing temperatures. The only exception was samples treated with PGMA and not annealed before acid grafting. Those samples demonstrated significantly higher CAs for TBP and hexadecane (Figs. 20 and 21). Figures 22 and 23 show surface energies of PFDOA- and PFHXA-treated surfaces that were annealed at different temperatures. Non-annealed PFDOA-
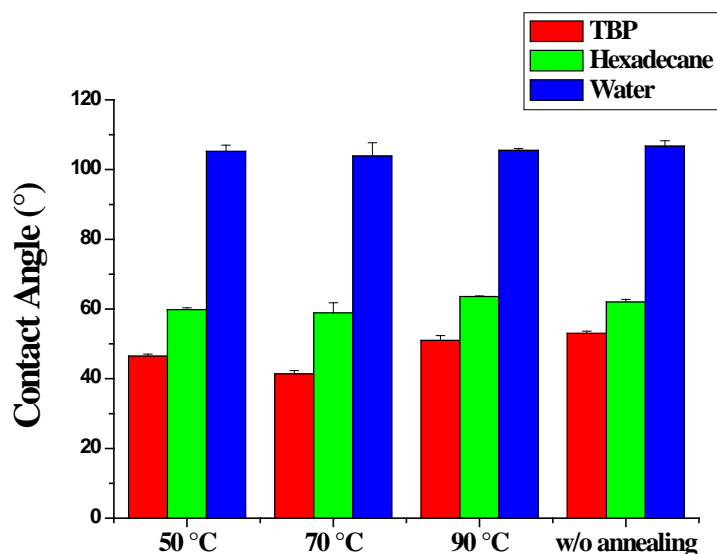
Figure 20. Contact Angles of TBP ( ), Hexadecane ( ) and Water ( ) on PFHXA-Treated Silicon Wafers (PGMA Annealed at Different Temperatures

22
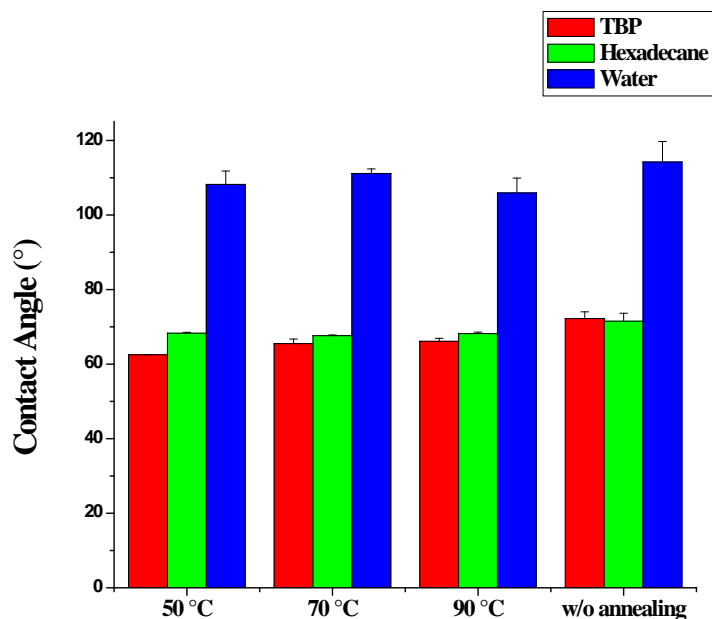
Figure 21. Contact Angles of TBP ( ), Hexadecane ( ) and Water ( ) on PFDOA-Treated Silicon Wafers (PGMA Annealed at Different Temperatures)

Figure 22. Surface Energy of PFDOA-Treated PGMA Surfaces

treated surfaces exhibited the lowest surface energy but the PFHXA-treated surface that was annealed at 90 °C, had the lowest surface energy. It was found that CA of TBP on PFHXA surfaces was always lower than on corresponding PFDOA surfaces.

Figure 23. Surface Energy of PFHXA-Treated PGMA Surfaces

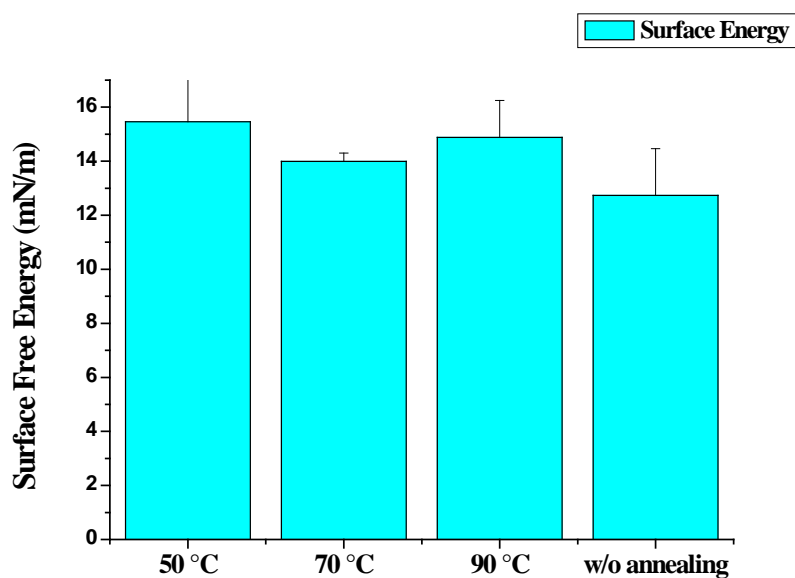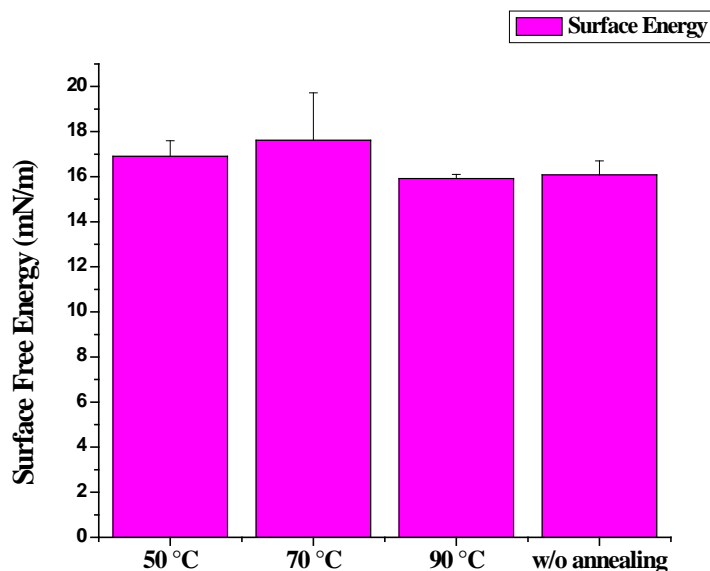## 4.14. Synthesis of Swellable in TBP Polymers as Models for CWA Sinks

Polymers swellable in TBP were synthesized and tested as model layers able to trap TBP within the layer. Poly(butyl methacrylate) (PBMA), which was synthesized from butyl methacrylate (purchased from Acros Organics), and poly(*tert*-butyl acrylate) (PTBA), purchased from Polymer Source, Inc., were tested for swelling with TBP. To compare their swelling capacity, PGMA-coated Si wafers were dip coated with either PBMA or PTBA solution consisting of 5% polymer and 0.15% UV radical initiator (benzophenone). MEK was used as solvent for PBMA deposition and acetone was used for PTBA. Deposited polymer layers were crosslinked via UV irradiation and rinsed in a solvent to remove any non-crosslinked polymer. Initial screening demonstrated that PBMA is much more swellable in TBP, and thus it was used in further experiments. Duration of UV treatment on PBMA swelling with TBP was studied. In these experiments, PBMA films of approximately 120 μm thickness were UV treated for 1, 2 and 4 h. The UV-treated PBMA layer was immersed into TBP for 24 h. The amount that TBP swells PBMA, calculated by difference in weight of swollen and dry samples, is shown in Table 4. It was found that swelling of the PBMA in TBP increased with increase in duration of UV treatment. Observed facts can be interpreted to indicate that PBMA on samples was not fully crosslinked during UV treatment and partially dissolved in TBP during swelling experiments.

Table 4. Weight of PBMA before and after Swelling with TBP*

UV Treatment	PBMA (mg)	PBMA with TBP (mg)	TBP Swollen (mg)	% Swelling
1 hour	19.4	25.2	5.8	29.90
2 hours	10	26.5	16.5	165.00
4 hours	17.1	62.5	45.3	264.71

* Measurements were performed on one sample

4.15. Robustness of the Coatings Made from PFDOA-Treated PGMA

Robustness of the PFDOA-treated PGMA coatings was tested. For this purpose, samples of PGMA-coated Si wafers were vapor treated with PFDOA at 120 °C for different times. A PGMA reference sample annealed at 120 °C for 17 h was prepared also. Surface morphologies and stiffness of the samples were investigated with AFM in tapping mode and in force volume (FV) mode, respectively. Subsequently, their Young's moduli were estimated. Also, CAs of TBP, hexadecane and water on the samples were measured and surface energies were calculated. A direct measure of the mechanical robustness (e.g., response to deformation) of coatings is extremely helpful to determine possible applications in the industry. For example, it has been shown that the lack of mechanical strength in coatings leads to deformation and subsequent delamination when a force is applied.

Surface topography of the coatings was analyzed by AFM in tapping mode, Figure 24. It was found that roughness of the coatings increased after the longer PFDOA treatment. AFM FV measurements showed significant difference between the reference PGMA sample and the sample treated for 1 h. The reference sample is significantly stiffer than the PFDOA-treated samples. This implies that PFDOA treatment causes the PGMA layer to be softer. Increasing PFDOA treatment time from 1 to 4 h causes (i) coatings to become softer and (ii) their uniformity to decrease.

Young's moduli (E) of coatings treated with PFDOA for different times were calculated using the FV Analysis Software. Log E (arbitrary units) is plotted against treatment duration for each sample, Figure 25. PFDOA caused the Young's modulus of coatings to decrease significantly after only 1 h of treatment. However, it was found that the stiffness of coatings did not change significantly if PFDOA treatments were longer.

Wettability of the coatings was measured with TBP, hexadecane and water. The results, shown in Figure 26, indicate that CAs for all solvents increase as the PFDOA treatment time increased. However, CAs do not change significantly after treatment for 4 h or longer. The surface energy of each PFDOA-treated sample was calculated using CAs of hexadecane and water. Figure 27 shows that the surface energy of samples decreased with increase of PFDOA treatment duration.

4.16. Fluorinated PGMA Copolymers by Solution Grafting of PFDOA

PGMA was modified with PFDOA in solution. The graft-copolymer (F-PGMA) obtained was used to modify model Si wafer surfaces. The F-PGMA copolymers were prepared by solution reaction of PGMA with 10, 20 and 30 % molar PFDOA. To do this, PGMA and PFDOA were mixed in MEK and shaken for 3 days. Next, the solutions were mixed with diethyl ether to precipitate F-PGMA copolymers. Finally, centrifuging was done at 5000 rpm for 15 min to remove the unreacted PFDOA from the copolymers. This treatment was conducted three times. Then, Si wafers were dip-coated with the F-PGMA copolymer solution and annealed at 80, 110 and 130 °C for different times. After the coating cooled, CAs of TBP, hexadecane and water on the different F-PGMA copolymer samples were measured and effective surface energies were calculated. CA data presented in Figure 28 indicate that initial CAs for water increase with

increasing mole fraction of PFDOA in the copolymer. CAs of water were measured after F-PGMA films were annealed for 1, 2, 4 and 6.5 h.

PGMA

PFDOA (1h)

PFDOA (2h)

PFDOA (4h)

PFDOA (17h)

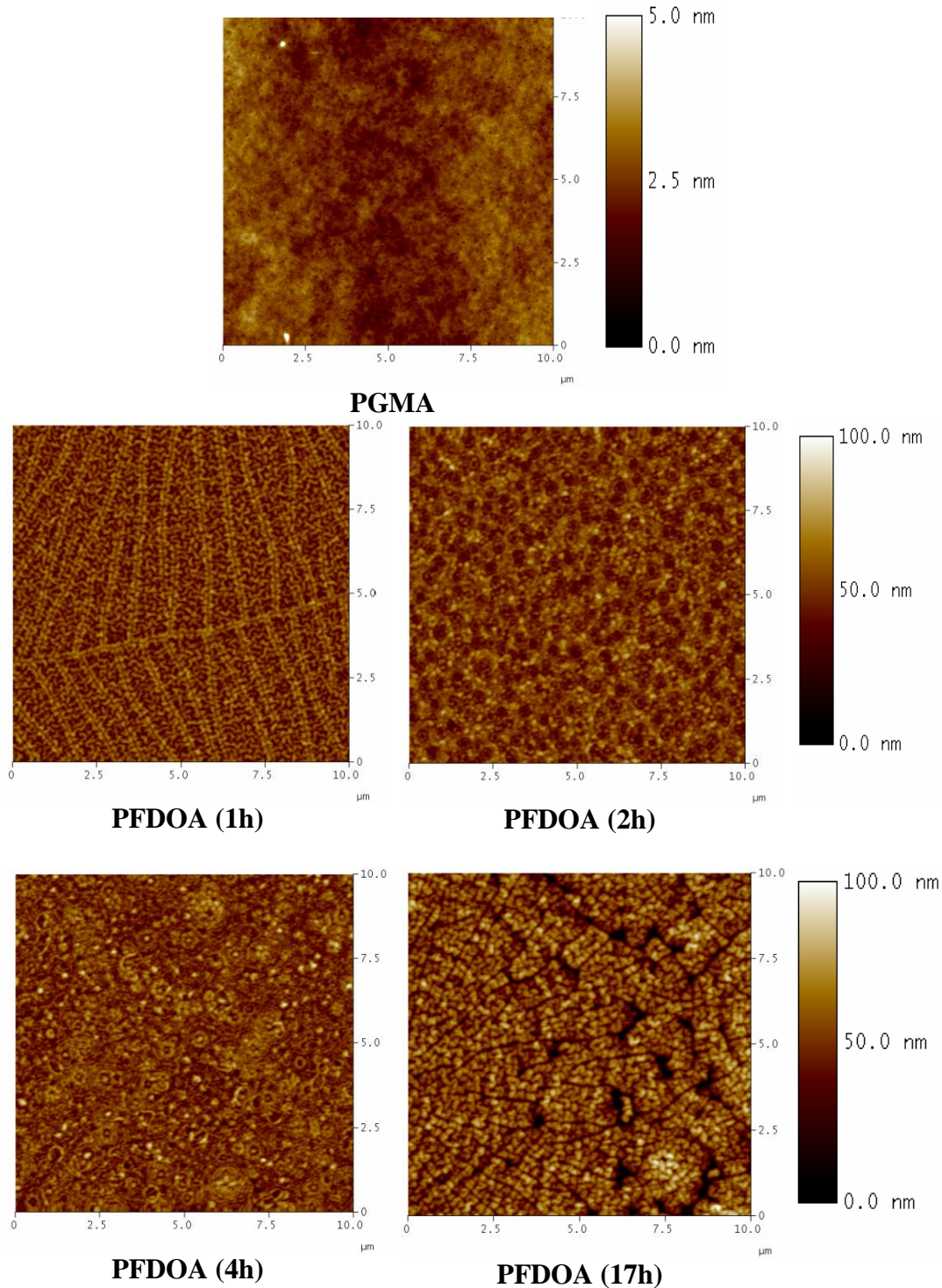**Figure 24. Surface Topography of Reference PGMS Coating and PFDOA-Treated Coatings for Different Treatment Times; Image Size is 10x10 μm**
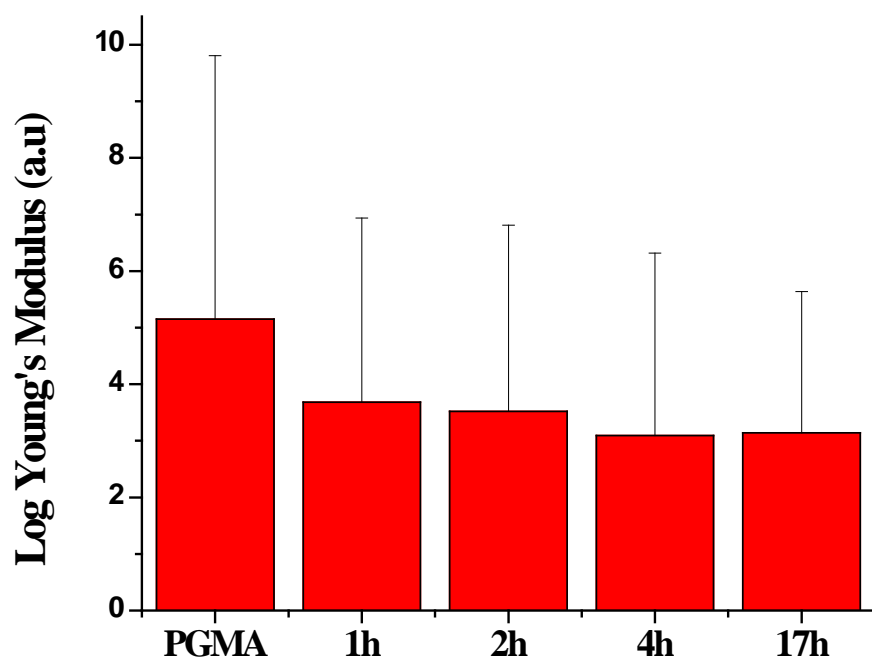
Figure 25. Logarithm of Young's Modulus (Arbitrary Units) of Reference (PGMA) Coating and PFDOA-Treated PGMA Coatings for Different Times
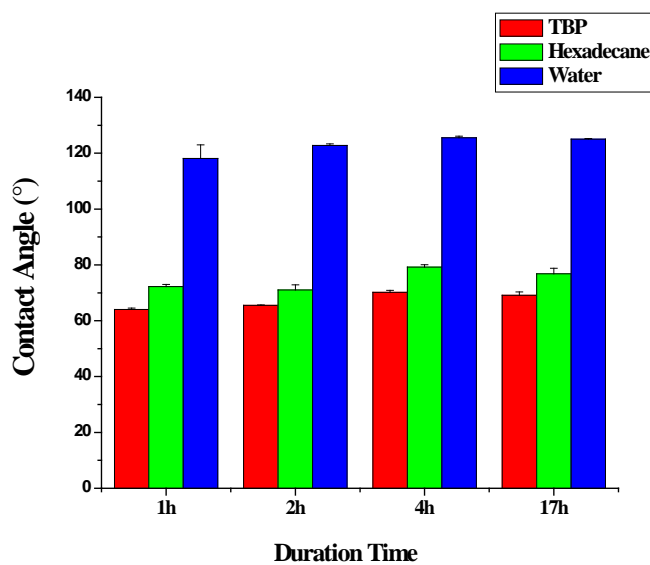

Figure 26. Contact Angles of TBP, Hexadecane and Water on PGMA Coatings Treated with PFDOA for Different Times
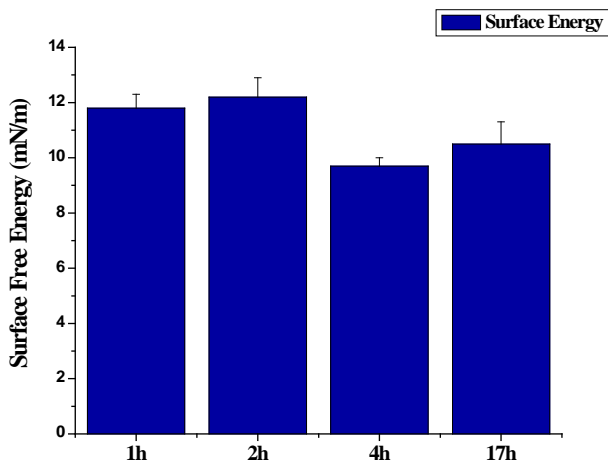
Figure 27. Surface Energy of PGMA Coatings after PFDOA Treatment for Different Times

Figure 28. Contact Angle of Water Measured on F-PGMA Films with Different PFDOA Content after Annealing at 80 °C for Different Times
Films were deposited on Si wafer surface.

To investigate the effects of annealing temperature on F-PGMA surface wettability, F-PGMA samples were annealed at 80, 110 and 130 °C for 6.5 h and rinsed with MEK overnight. The CAs of TBP, hexadecane and water on all samples, which were annealed at 80, 110 and 130 °C for 6.5 h, are shown in Figures 29–31, respectively. The highest CA of TBP on F-PGMA surfaces was found to be 35° on films annealed at 130 °C. The surface energy of F-PGMA layers, calculated using CAs of hexadecane and water, is shown on Figure 32. The surface energy of all samples is close to or higher than the surface energy of hexadecane, 27.5 mN/m.
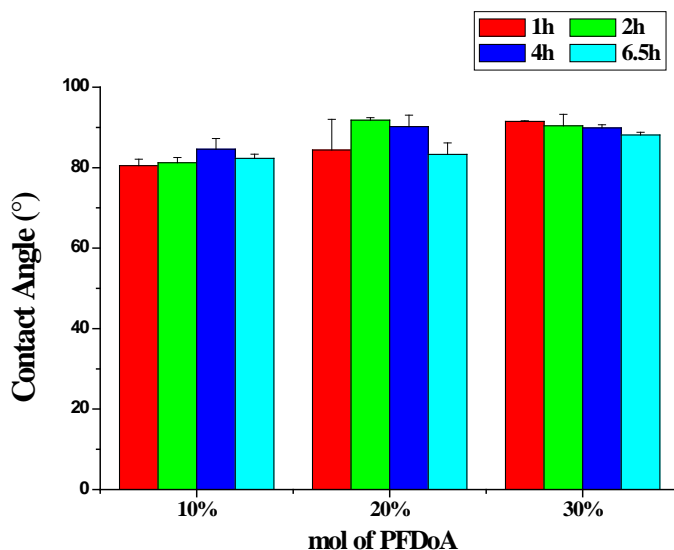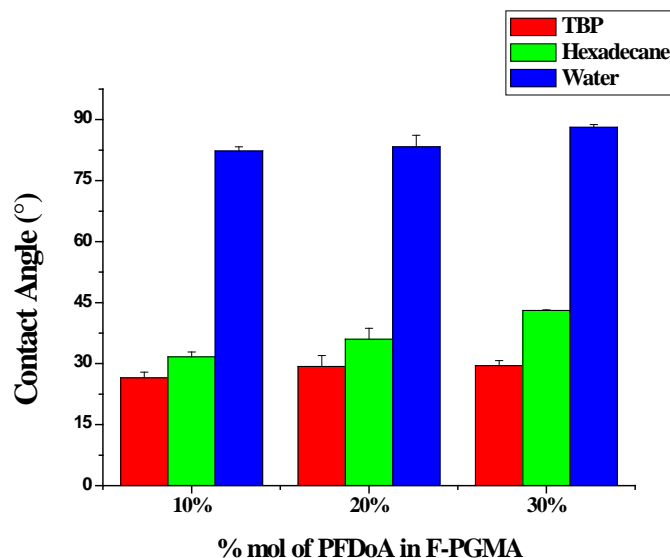
Figure 29. Contact Angles Measured on F-PGMA Films with Different PFDOA Content after Annealing at 80 °C for 6.5 h. Films were deposited on Si wafer surface.

Figure 30. Contact Angles Measured on F-PGMA Films with Different PFDOA Content after Annealing at 110 °C for 6.5h

4.17. Nanoparticle-filled Low-Surface-Energy Coatings

We have shown the maximum CAs of TBP, hexadecane and water on PFDOA-treated PGMA flat surfaces to be 72.2, 71.5 and 114.2°, respectively. Experiments were conducted to increase hydrophobicity/oleophobicity of silicon wafer surfaces coated with the PGMA layer containing nanoparticles, followed by PFDOA treatment. In these experiments, PGMA was mixed with either TiO_2, AlO(OH) or $Mg(OH)_2$ nanoparticles at different ratios. PGMA–nanoparticle suspensions were deposited onto Si wafer surfaces. Next, samples were PFDOA treated at 120 °C over-
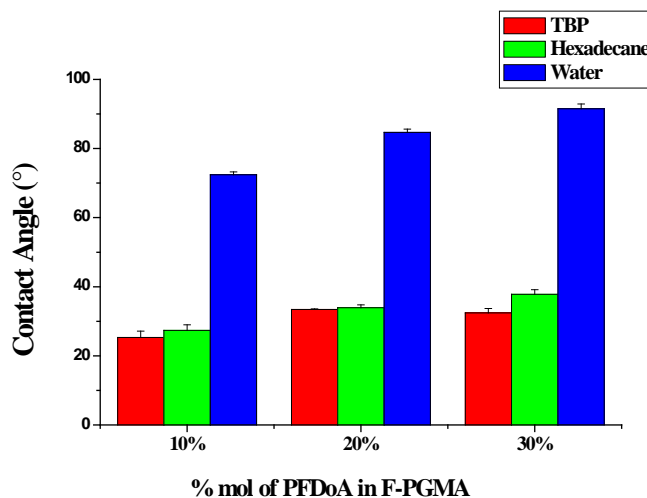
29
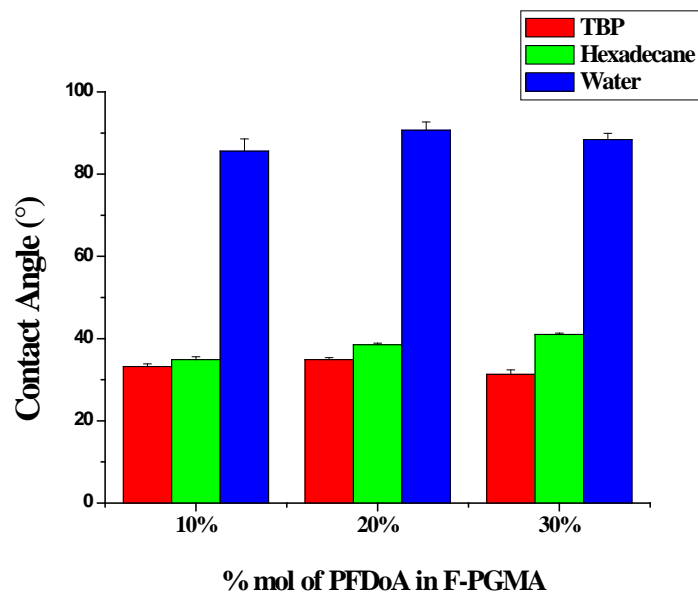
Figure 31. Contact Angles Measured on F-PGMA Films with Different PFDOA Content after Annealing at 130 °C for 6.5 h
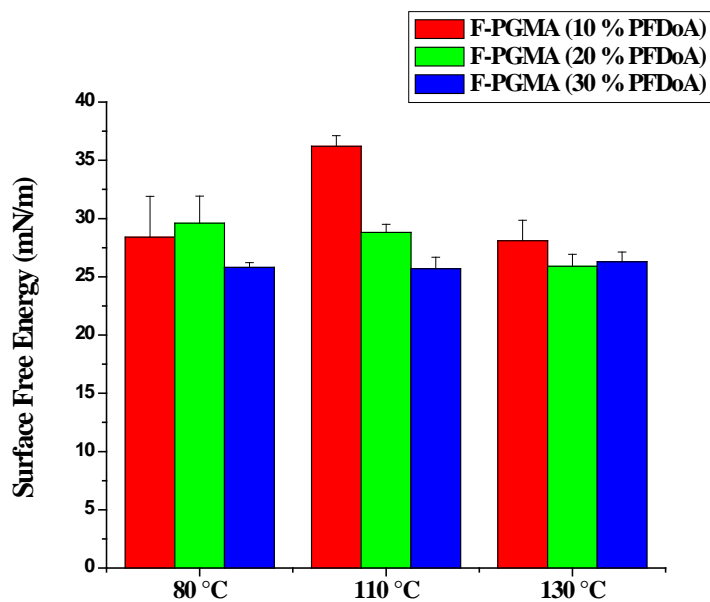

Figure 32. Surface Energy Calculated for F-PGMA Films with Different PFDOA Content after Annealing at 80, 110 and 130 °C for 6.5 h

night. The type of nanoparticles, PGMA-to-nanoparticles ratio and procedure of the suspension preparation were varied. Wettability of the coatings was tested with TBP, hexadecane and water.

4.17.1. TiO$_2$-Containing Coatings

To prepare the coatings Si wafers were spin coated at 500, 1000 and 1500 rpm using suspensions of TiO$_2$ nanoparticles dispersed in PGMA polymer solution in MEK. The ratio of TiO$_2$: PGMA was 3:2. After the PFDOA treatment of the samples, CAs of TBP, hexadecane and water were measured (Fig. 33). Coatings produced at low spin rates are rough and not uniform. With increasing spin rate more uniform distribution of TiO$_2$ within PGMA was obtained. Surface energies of samples were calculated using the CAs of hexadecane and water. It is shown in Figure 34 that the lowest surface energy was obtained when Si wafers were coated with 3:2 TiO$_2$: PGMA solution at 500 rpm.
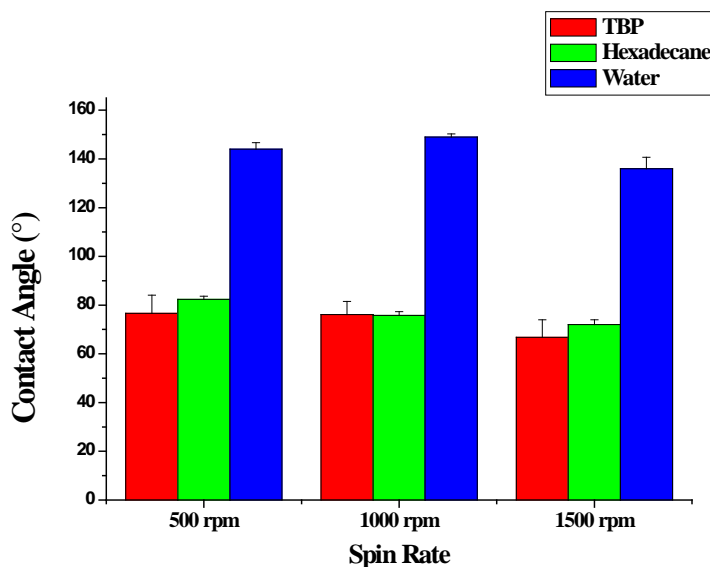

Figure 33. Contact Angles of TBP, Hexadecane and Water on Si Wafer Surfaces Coated with TiO$_2$ Suspension in PGMA (3:2) Solution at Different Spin Rates.
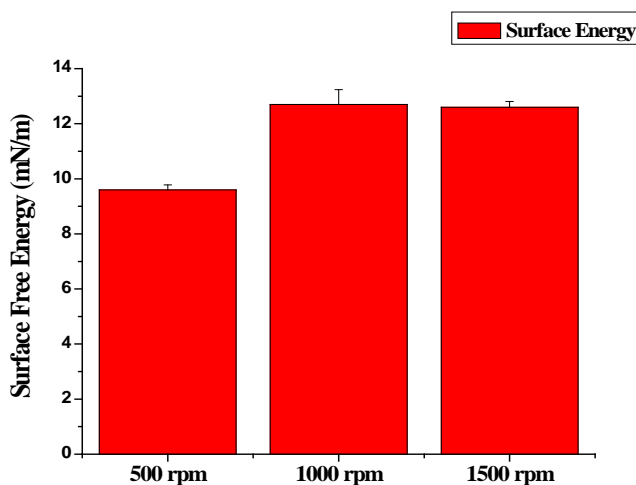

Figure 34. Surface Energy of the Si Wafer Surfaces Coated with TiO$_2$ Suspension in PGMA (3:2) Solution at Different Spin Rates

31

We have also varied the ratio of titania to PGMA in the coatings. The ratios of TiO_2 to PGMA utilized for coatings preparation were 1.5:1, 2:1 and 5:1. Si wafers were spin coated at 1000 rpm using suspensions of TiO_2 nanoparticles dispersed in PGMA polymer solutions prepared from MEK, followed by PFDOA treatment. Figure 35 shows that the compositions with the largest amount of nanoparticles exhibit the largest CAs. The surface energies of the coatings were calculated and the coating with TiO_2–PGMA ratio 5:1 has the smallest value, 8.97 mN/m (Fig. 36). Morphology of the coatings is shown in Figure 37.
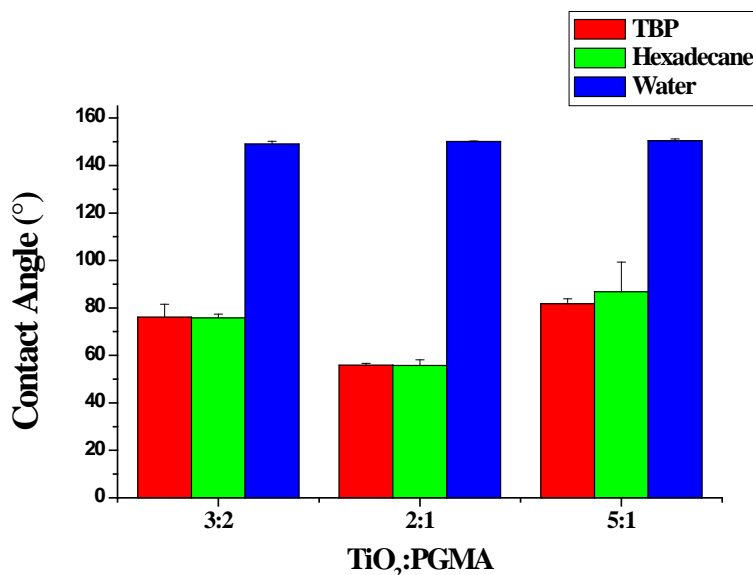

Figure 35. Contact Angles of TBP, Hexadecane and Water on Si Wafer Surfaces Coated at 1000 rpm with Different TiO_2 Suspensions in PGMA Solution
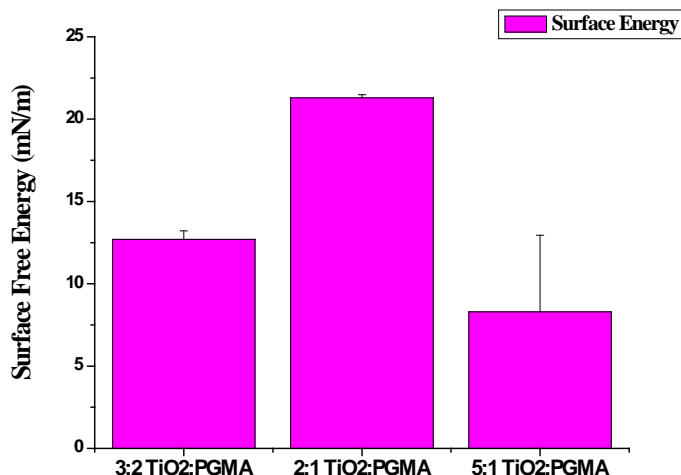

Figure 36. Surface Energy of Si Wafer Surfaces Coated at 1000 rpm with Different TiO_2 Suspensions in PGMA Solution

3:2 TiO$_2$:PGMA @1000 rpm
RMS: 230 nm
Surface area: 806.434 μm^2

2:1 TiO$_2$:PGMA @ 1000 rpm
RMS: 241 nm
Surface area: 823.906 μm^2

5:1 TiO$_2$:PGMA @ 1000 rpm
RMS: 229 nm
Surface area: 840.644 μm^2
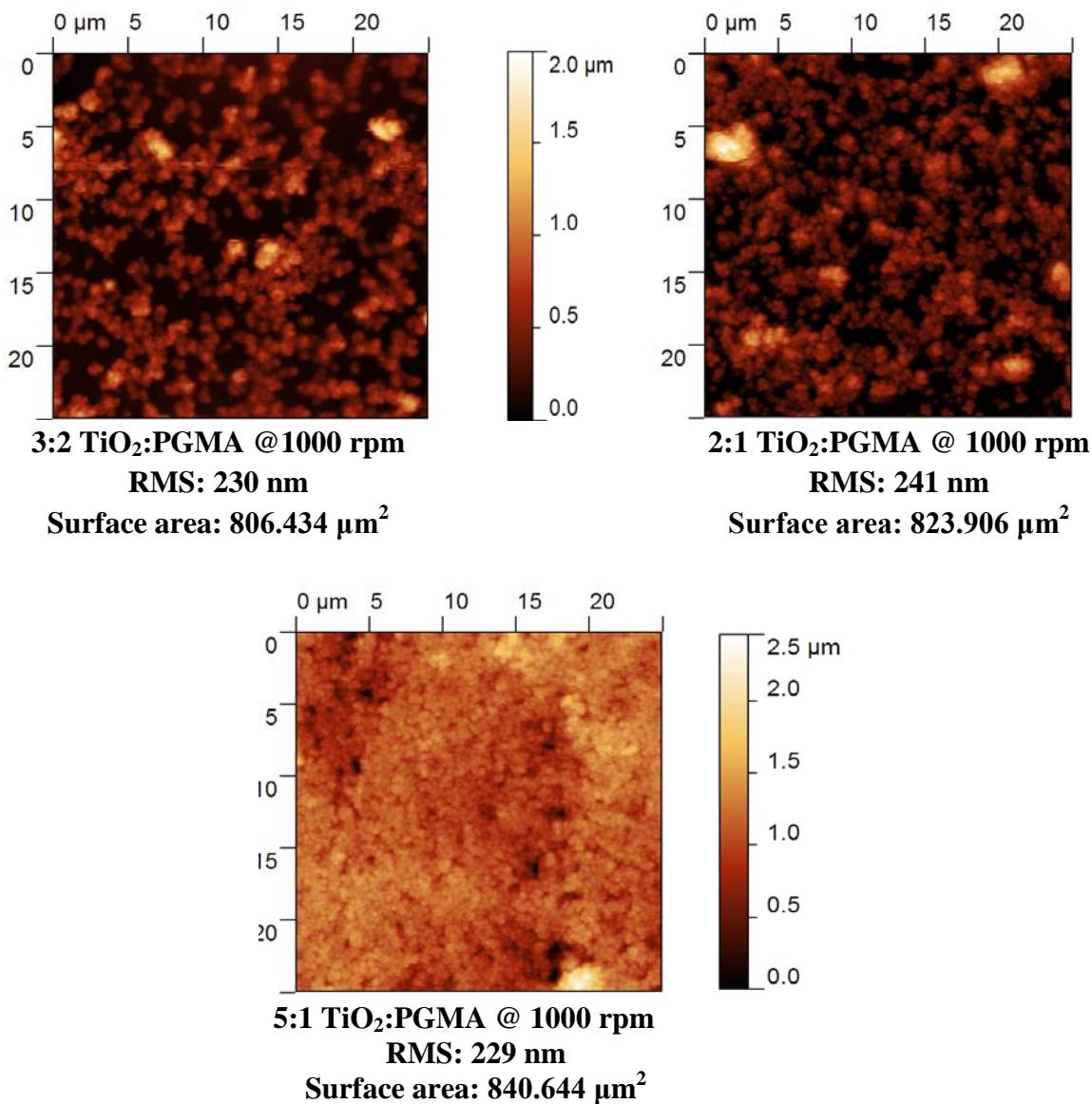
Figure 37. AFM Images of Si Wafers Spin Coated with TiO$_2$ Suspensions in PGMA Solution with Different Nanoparticle-to-PGMA Ratios
RMS indicates roughness.

4.17.2. AlO(OH)- and Mg(OH)$_2$-Containing Coatings

AlO(OH) and Mg(OH)$_2$ nanoparticles were utilized to prepare the LSE coatings. For this purpose nanoparticles were dispersed in the PGMA solution in MEK. The obtained suspensions were dip-coated onto the surface of the Si wafers followed by vapor treatment with PFDOA. The ratio between nanoparticles and PGMA was varied. It was 2:1 and 4:1 for AlO(OH) and 0.8:1, 1:1 and 2:1 for Mg(OH)$_2$. CAs of the coatings is shown in Figures 38 and 39. The lowest wettability of the coatings was obtained for a nanoparticle-to-PGMA ratio of 2:1 for AlO(OH) and 1:1 for
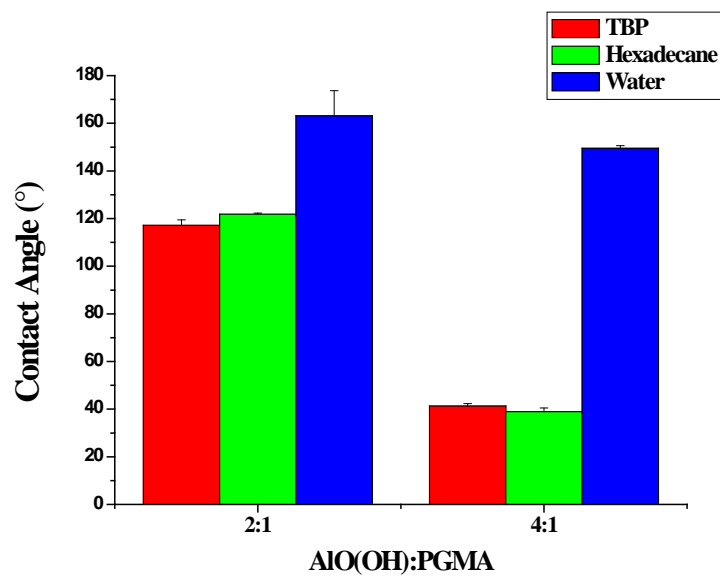
Figure 38. Contact Angles of TBP, Hexadecane and Water on Si Wafer Surfaces Coated with Different AlO(OH) Suspensions in PGMA Solution and Mixed at Different Ratios
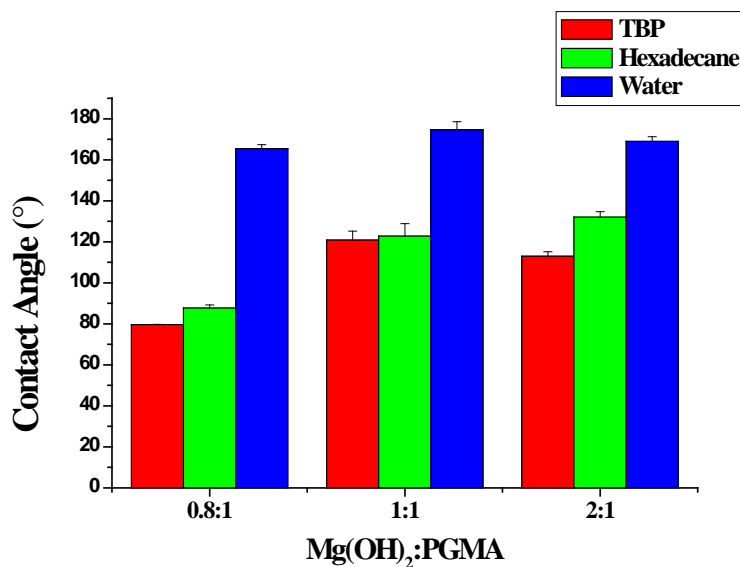
Figure 39. Contact Angles of TBP, Hexadecane and Water on Si Wafer Surfaces Coated with Different Mg(OH)$_2$ Suspensions in PGMA Solution and Mixed at Different Ratios

Mg(OH)$_2$. Surface energy of the coatings was calculated and shown on Figures 40 and 41. The lowest surface energy calculated for AlO(OH) was 1.89 mN/m and 1.36 mN/m for Mg(OH)$_2$.
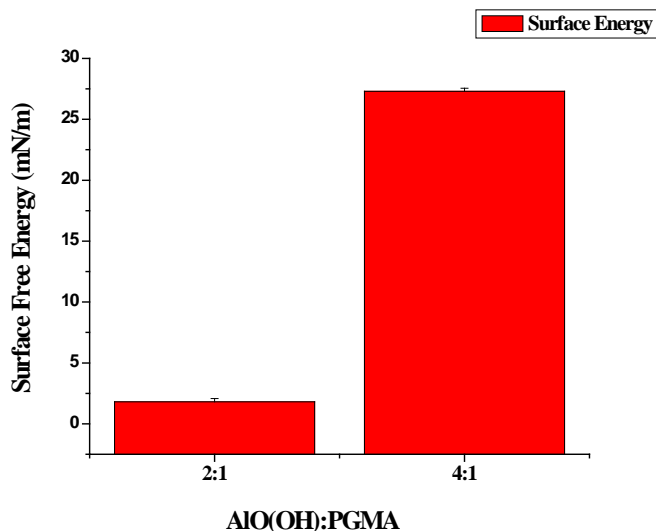
Figure 40. Surface Energy of Si Wafer Surfaces Coated with Different AlO(OH) Suspensions in PGMA Solution and Mixed at Different Ratios
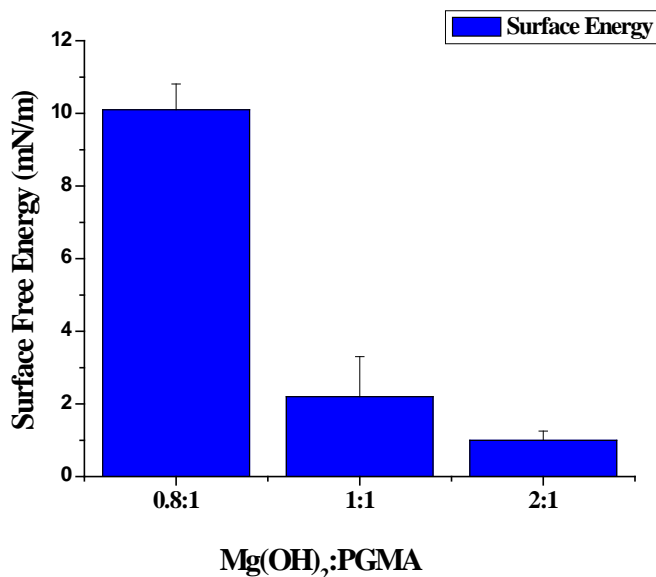
Figure 41. Surface Energy of Si Wafer Surfaces Coated with Different $Mg(OH)_2$ Suspensions in PGMA Solution and Mixed at Different Ratios

To investigate the influence of the coating roughness on the coating wettability and surface energy, coatings with different nanoparticles to PGMA ratios were prepared. Boehmite (AlO(OH)) was used to increase roughness of the coatings. Specifically, silicon wafer surfaces were coated with PGMA solution mixed with AlO(OH) nanoparticles in different ratios from1:1 to 8:1 in MEK. Suspensions of nanoparticles in PGMA solutions were shaken for 25 days.

Sets of samples were made on the 5th, 14th, and 25th day. Then, AlO(OH)–PGMA coatings were modified by PFDOA vapor treatment at 120 °C overnight. CAs of TBP, hexadecane and water on rough surfaces after PFDOA treatment were measured. Effective surface free energy was calculated based on the CAs of water and hexadecane for the coatings. Figure 42 shows the CAs of TBP, hexadecane and water on PFDOA-treated AlO(OH)–PGMA coatings after shaking suspensions for 5, 14 and 25 days, respectively.

Figure 42. CAs of TBP, Hexadecane and Water on PFDOA-Treated AlO(OH)–PGMA Coatings after Shaking Suspensions for 5 (top left), 14 (top right) and 25 days (bottom)

It was found that the wettability of AlO(OH)–PGMA coatings was influenced by both AlO(OH):PGMA ratios and duration of shaking of AlO(OH)-PGMA suspension. When the AlO(OH)–PGMA ratio was increased from 1:1 to 8:1, wettability of coatings decreased as can be seen from the increase in CAs of TBP, hexadecane and water on coatings from 90°, 92° and 143° to 127°, 129° and 165°, with ± 3° errors (Fig. 42). Effective surface energies of the AlO(OH)–PGMA-based coatings calculated using CAs of hexadecane and water are presented in Figure 43. The lowest surface energy, 1.09 mN/m, was obtained using an 8:1 AlO(OH):PGMA
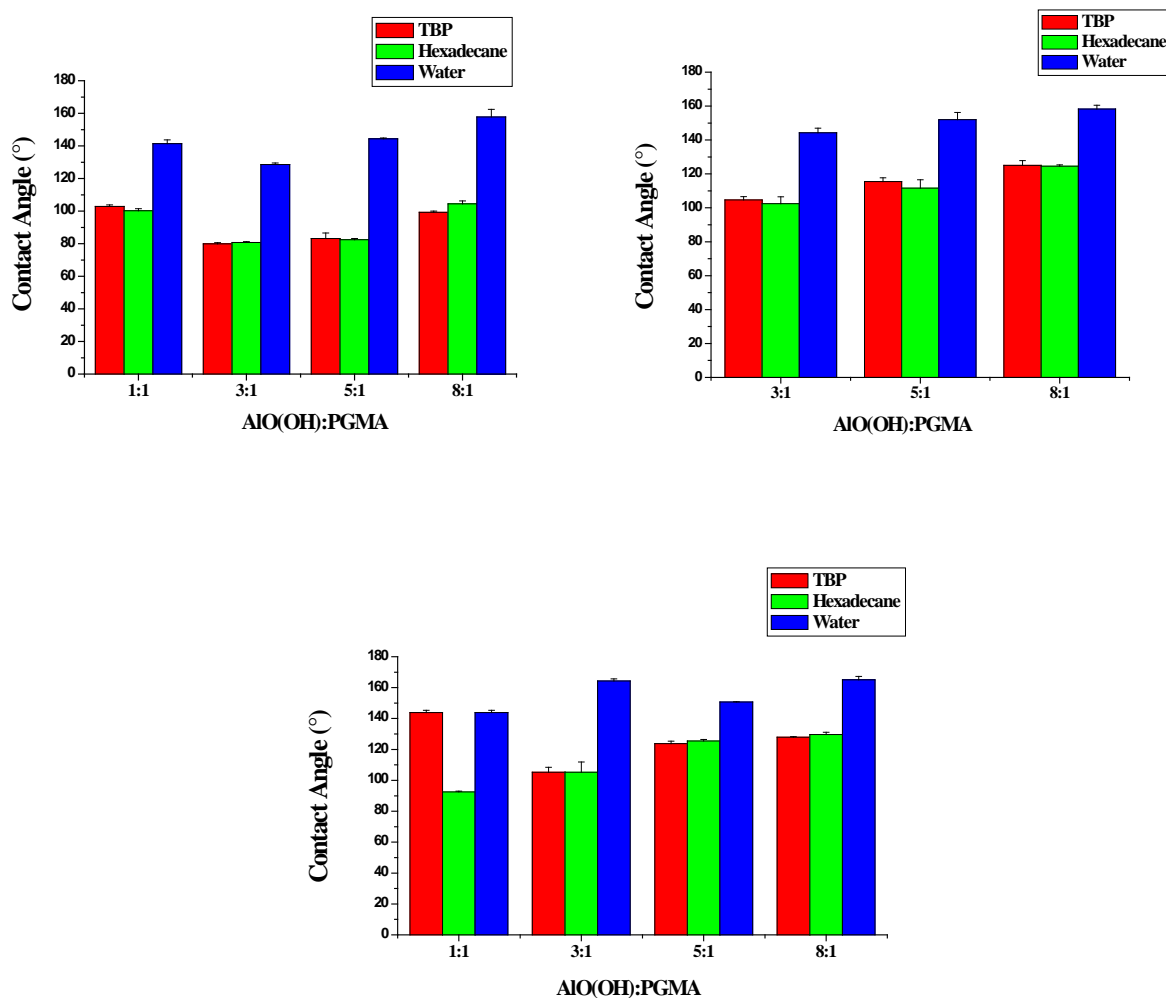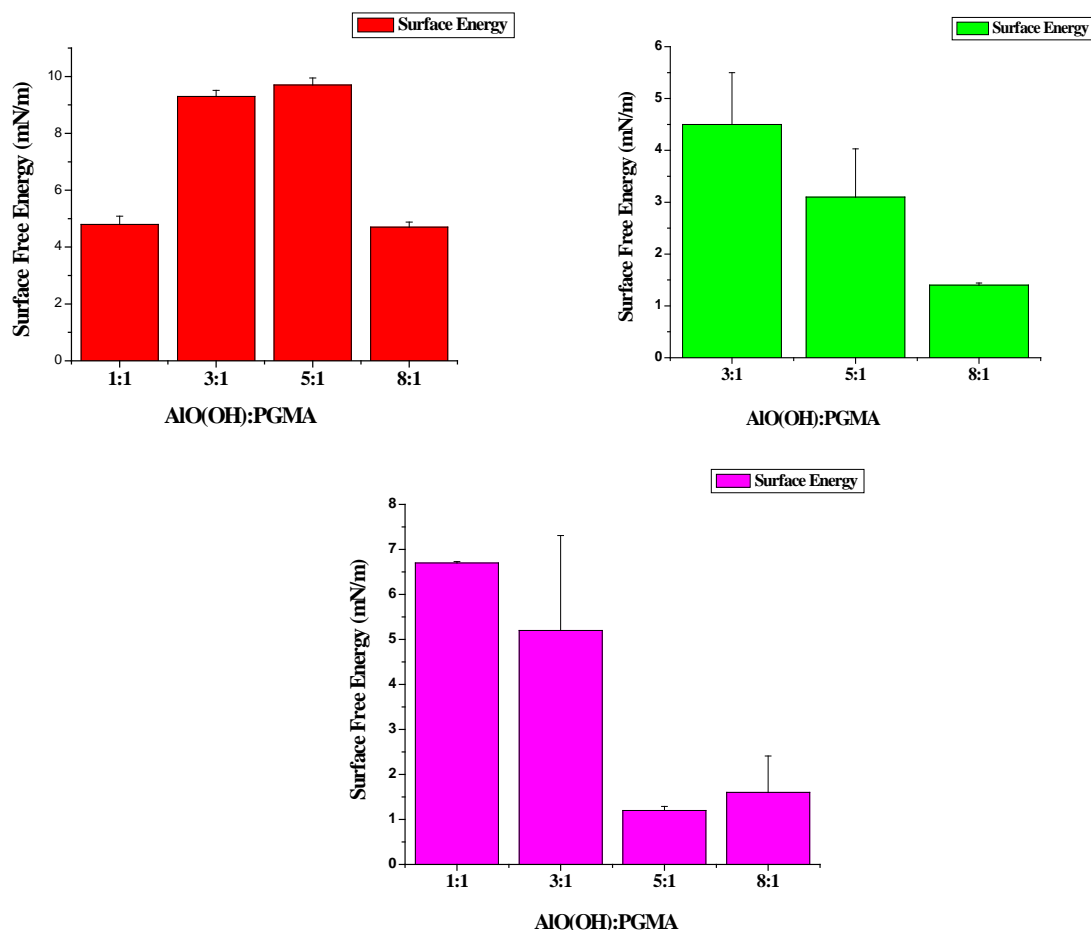
36

Figure 43. Surface Energy of PFDOA-Treated AlO(OH)–PGMA Coatings after Shaking Suspensions for 5 (top left), 14 (top right) and 25 days (bottom)

suspension after shaking for 25 days. Indeed, addition of the particles resulted in higher surface roughness. AFM imaging was not possible because of the high surface roughness. Because of this, profilometry was used to analyze the coating surfaces. Representative profilometer cross-sections of AlO(OH)–PGMA coatings are shown in Figures 44 and 45.

Duration of AlO(OH) shaking in PGMA solution also affected wettability of the coatings. We found that AlO(OH) did not disperse well in PGMA solution after being shaken for 5 days. Because of this, coatings obtained using AlO(OH):PGMA suspension in different ratios were rough but not uniform. Increasing the duration of shaking from 5 to 14 and 25 days produced better-dispersed suspensions, and more uniform layers were obtained. The most homogeneous suspensions were obtained after shaking for 25 days, thus resulting in the most-uniform coatings. The CAs of TBP on AlO(OH)–PGMA coatings with 8:1 ratio increased from 99° to 125° and 127° for the suspension prepared for 5, 14 and 25 days, respectively.

Nanoparticle addition to the PGMA treated with PFDOA lead to an increase in the coating roughness and a substantial drop in the effective surface energy. In fact, some of the coatings

37

Figure 44. Profilometer Images of PFDOA-Treated AlO(OH)–PGMA Coatings after Shaking for 5 Days: a) RMS Roughness = 0.91 μm (1:1 AlO(OH):PGMA Suspension; b) RMS Roughness = 0.52 μm (8:1 AlO(OH):PGMA Suspension
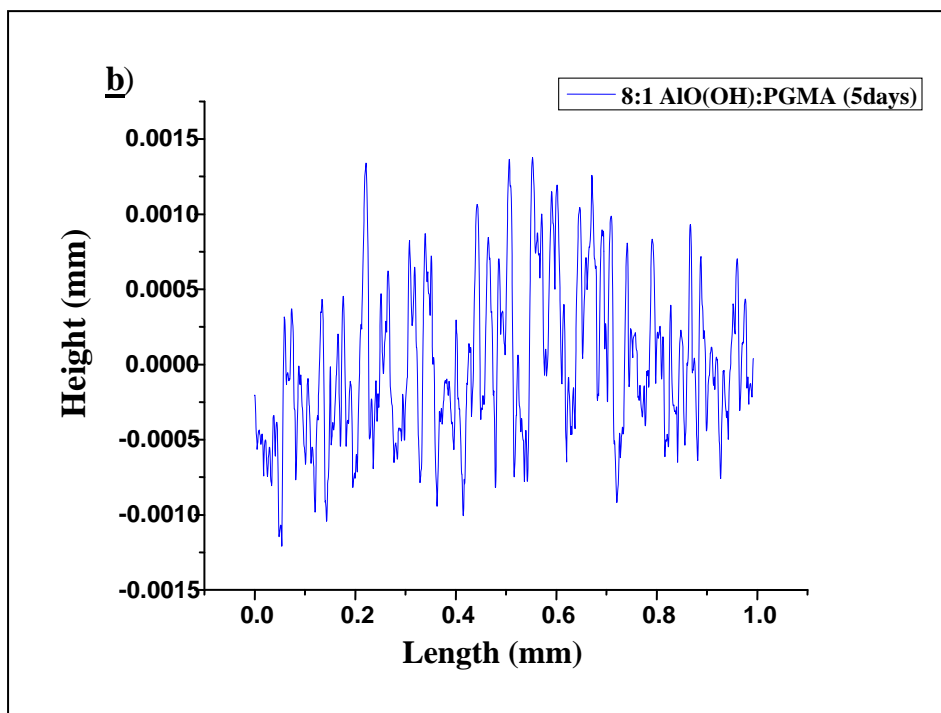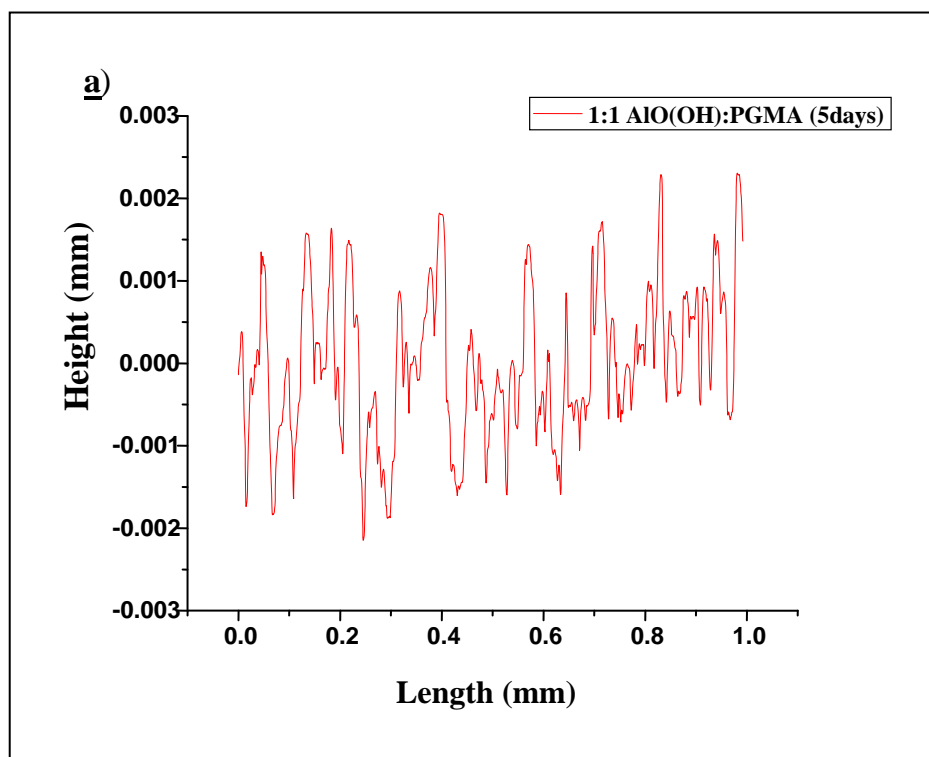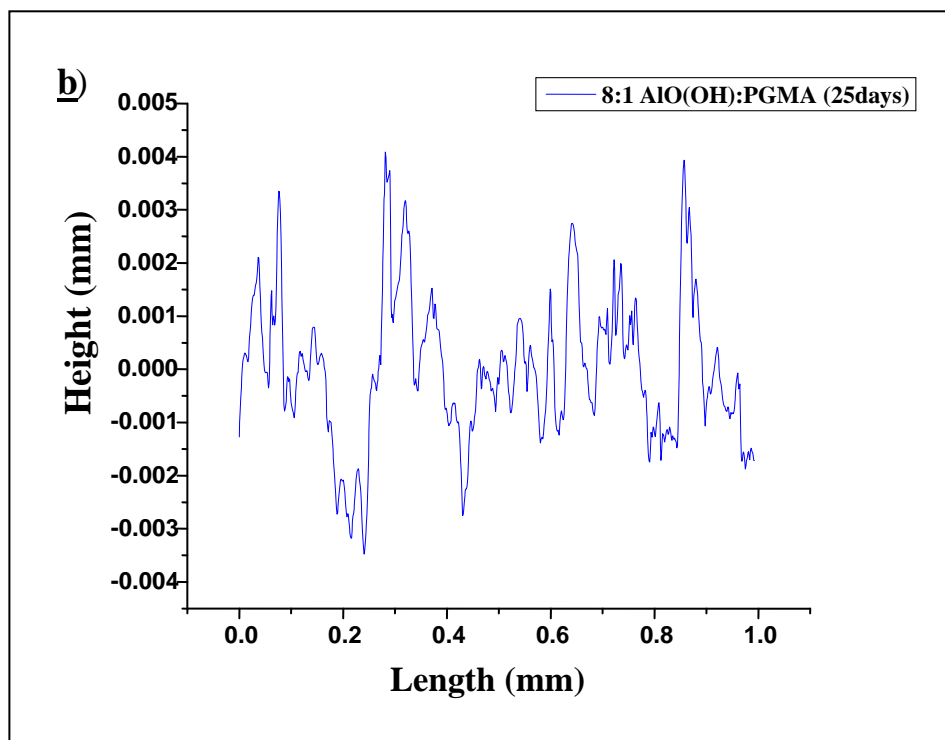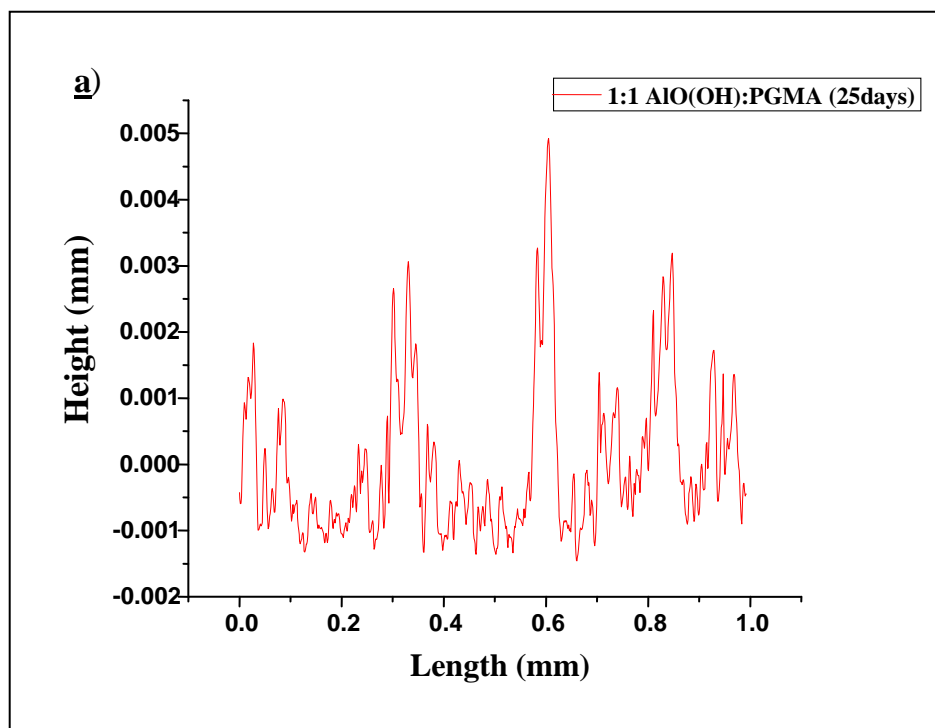
38

Figure 45. Profilometer Images of PFDOA-Treated AlO(OH)–PGMA Coatings after Shaking for 25 Days: a) RMS Roughness = 1.15 μm (1:1 AlO(OH):PGMA Suspension; b) RMS Roughness = 1.38 μm (8:1 AlO(OH):PGMA Suspension

demonstrated very low calculated surface energy, in the range of 1.1–2 mN/m. Also, TBP, which was used as a CWA simulant in our studies, demonstrates very high CAs on these coatings, reaching values of ~130°.

4.18. Liquid Penetration into Porous Materials

Several theories aim to explain interactions of liquids with materials having μm-size pores[5]. These theories assume that liquid penetrates the material and flows through it following Darcy's law. However, this flow scenario becomes questionable when the pore size decreases to nanometers. In this case, the material's permeability drops down significantly, and it is natural to assume that the drop would spread over the material, as it would be non-porous. Thus, Tanner's law should describe the expected spreading kinetics. $R \sim (\sigma t \Omega^3/\eta)^{1/10}$, where R is the radius of the drop base, Ω is volumetric flow rate, η is liquid viscosity, σ is surface tension, and t is time. Hence, the drop radius should scale as $t^{1/10}$. To check this hypothesis, we used nanoporous aluminum membranes (Whatman Anodisc 25). Membranes with three different pore sizes were tested, types 1, 2 and 3. Each membrane had different pore sizes on the bottom and top sides. Therefore, each membrane was tested twice, once on the bottom side and once on the top.

Step one of the experiments was to determine the kinetics of drop spreading for each membrane. In step two, using a membrane found in step one, we studied the effect of fluid viscosity on the kinetics of drop spreading. TBP, DEP and hexadecane were used in these experiments; properties are listed in Table 5.

Table 5. Properties of Tested Liquids

Fluid	Density (kg/m^3)	Surface Tension (mN/m)	Viscosity at 20 °C (mPa*s)	Vapor Pressure mm Hg
Water	1000	72.0	1.002	23.756
TBP	972	31.7	3.800	0.00409
DEP	1190	37.5	7.926	0.00210
Hexadecane	753	27.7	3.025	0.00500

Figure 46, the top view of a TBP drop on the alumina membrane having conical pores with large taper and the smallest pore openings, illustrates one of the major findings of this project. The drop was positioned on the drop cupola (a hemispherical cap) at the center, the first and second terraces surrounding the central spherical cap. Using a Raman microscope we studied the dynamics of terrace formation.

Using an atomic force microscope (AFM) (dimension 3100, Veeco Incorporation) and an environmental electron scanning microscope (ESEM) (Hitachi S4800) we analyzed the membrane surface and pore morphology. We confirmed that the pore size is a critical parameter controlling the spreading kinetics. The pore size, along with the membrane roughness, determines the formation of terraces, and the drop spreading behavior.

Figure 46. TBP Droplet on Nanoporous Alumina Membrane

4.19. Spreading Kinetics and Spreading Factors

The results of the image analysis of pore sizes and droplet volumes are shown in Tables 6 and 7. ImageJ (NIH) software was used to process the images.

Table 6. Pore Diameters

Membrane		Average Pore Diameter (nm)
Type	Side	
1	Top	39
	Bottom	192
2	Top	95
	Bottom	268
3	Top	164
	Bottom	273

Table 7. Average Droplet Volumes

Fluid	Droplet Volume V_0 (µL)
TBP	0.0162
DEP	0.0093
Hexadecane	0.0062

To calculate the spreading factor, we used the diameter of the outmost terrace, D_f, occupied by the droplet after 2 min. D_i is initial diameter of the droplet calculated from the measured droplet volume, $D_i = (3V_0/4\pi)^{1/3}$. The spreading factor was defined as $S = D_f / D_i$. The 2-min time interval was used because after 2 min the drop diameter did not appreciably increase (Figs. 47–49).

The first set of experiments revealed two possible types of drop spreading kinetics. The first is $t^{1/2}$ kinetics, found on the bottom side of the type 1 membrane with 192-nm pore opening. All other membranes showed Tanner's law kinetics. Figure 50 shows the membrane that has the best representation of $t^{1/2}$ kinetics. The blue line and the red dots line up on the type 1 bottom side membrane. Figures 50–51 confirm the Tanner kinetics for the droplet spreading on other membranes.
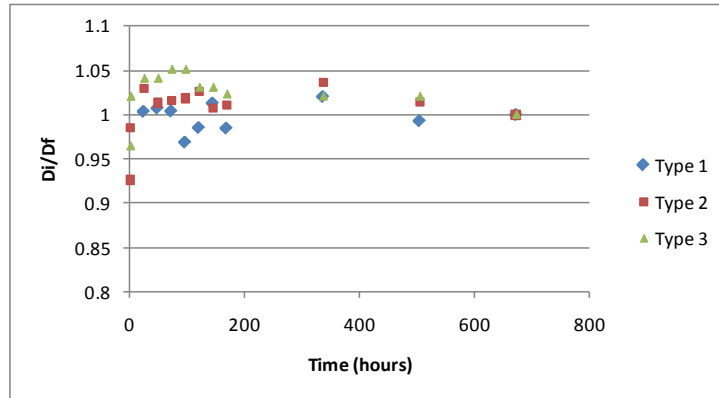
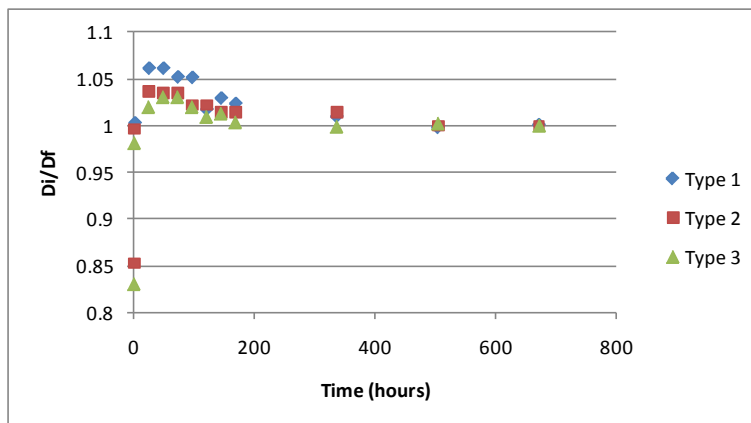**Figure 47. TBP on Top Side of Type 1, 2, 3 Membranes**

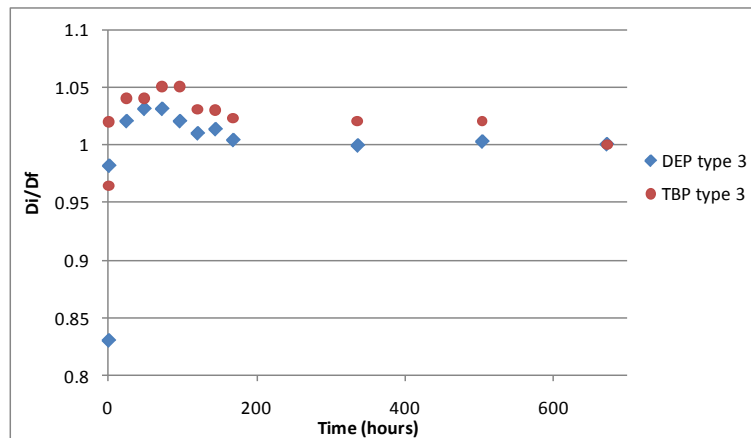**Figure 48. DEP on Top Side of Type 1, 2, 3 Membranes**

Figure 49. TEB and DEP on Type 3 Membrane

Figure 50. Spreading Kinetics of the Outer Terrace; TBP on Type 1 Membrane, Bottom and Sides, Respectively

Figure 51. Spreading Kinetics of the Outer Terrace; TBP on Type 2 Membrane, Bottom and Sides, Respectively

43
Distribution A: Approved for public release; distribution unlimited.
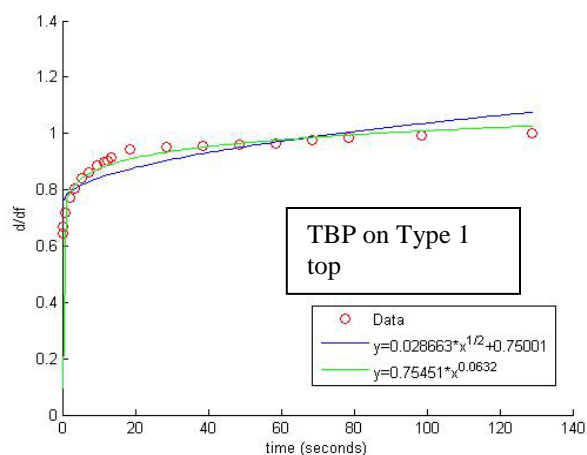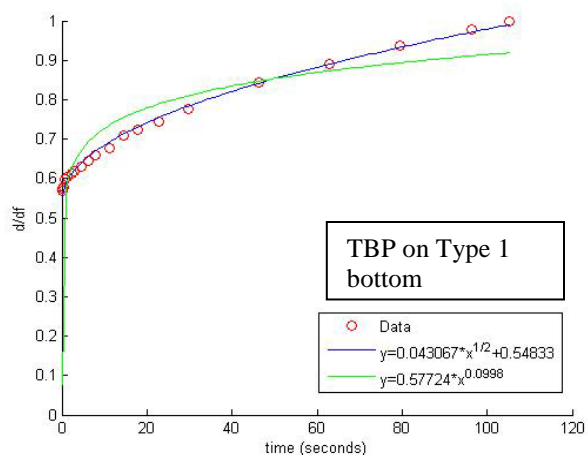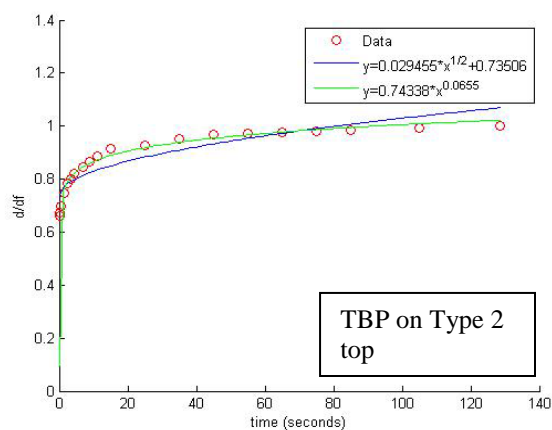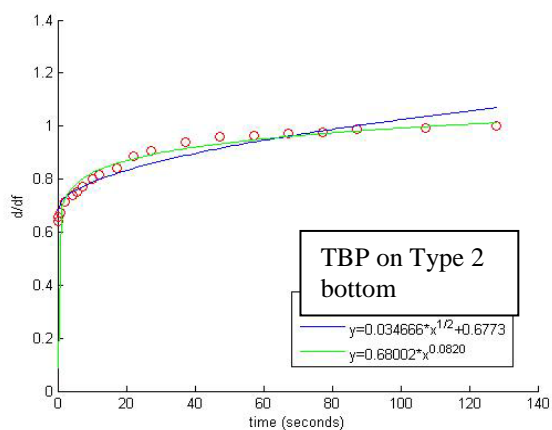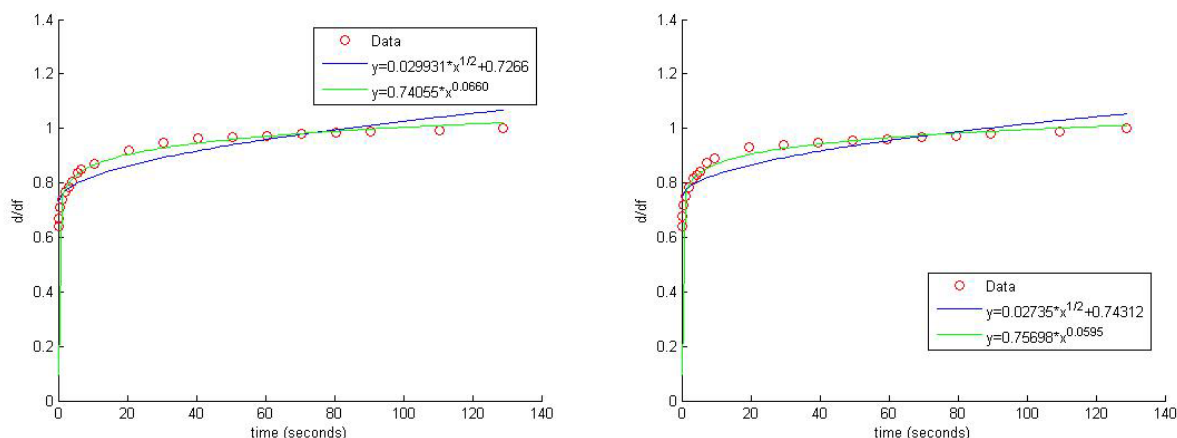88ABW-2011-6233, 30 November 2011.

Figure 52. Spreading Kinetics of the Outer Terrace; TBP on Type 3 Membrane, Bottom and Top Sides, Respectively

In the second set of experiments, we examined the spreading kinetics of different liquids. Figure 53 shows the spreading kinetics of a hexadecane droplet. The hexadecane results roughly match up with TBP because they have similar liquid properties, in terms of surface tension, viscosity and vapor pressure. On the other hand, DEP closely followed Tanner's law, most likely because of the viscosity effect. DEP is twice as viscous as TBP and hexadecane.
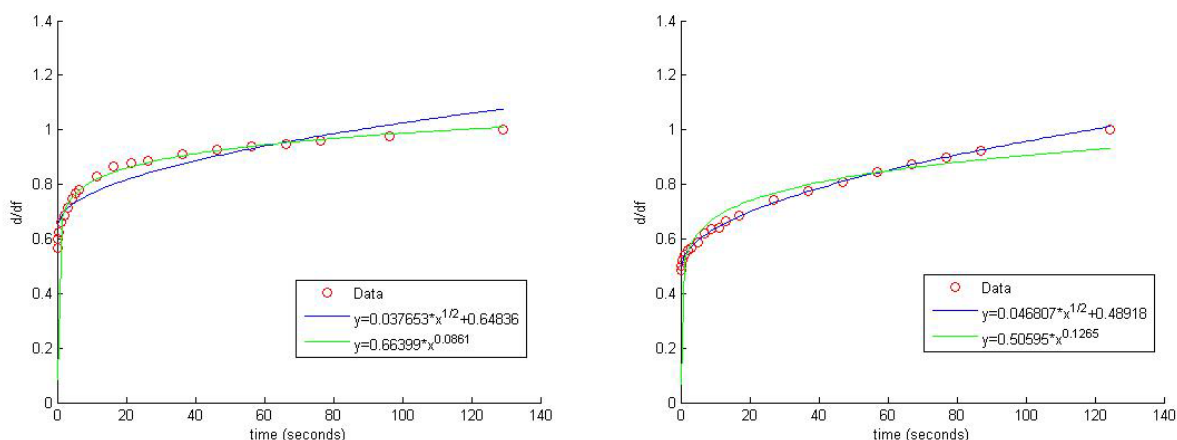
Figure 53. Spreading Kinetics of the Outer Terrace; DEP and Hexadecane on the Bottom Side of Type 1 Membrane

Table 8 shows different spreading factors of these three liquids. Hexadecane has the largest spreading factor of the three, and TBP had the smallest spreading factor. The Type 3 bottom side membrane had the largest spreading factor, and Type 2 top side membrane had the smallest. This tendency correlates with the spreading areas as defined in Figure 54.

Table 8. Spreading Factors of Different Droplets on Different Membranes

Membrane		Challenge	Spreading Factor $(S = D_f /D_i)$
Type 2	Top	TBP	2.88

	Bottom		3.72
Type 3	Top		4.18
	Bottom		4.61
	Top		3.60
Type 1	Bottom		3.55
			3.98
		Hexadecane	4.16

4.20. Membrane Morphology and Spreading Mechanism

Examination of the surface and pore morphology of different membranes (Figs. 55–56) shows that the pores in the membranes are not perfectly cylindrical, but that they taper from one side of the membrane to the other. Figure 57 shows the side view of the Type 1 membrane. The pores do
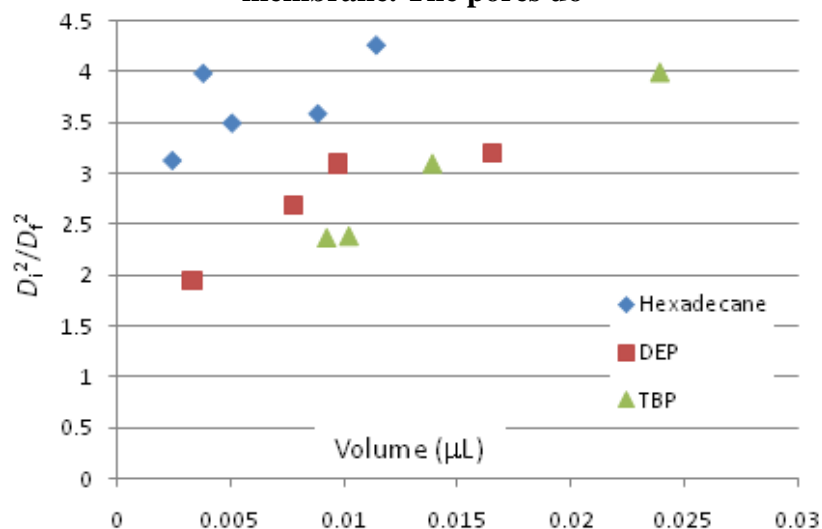

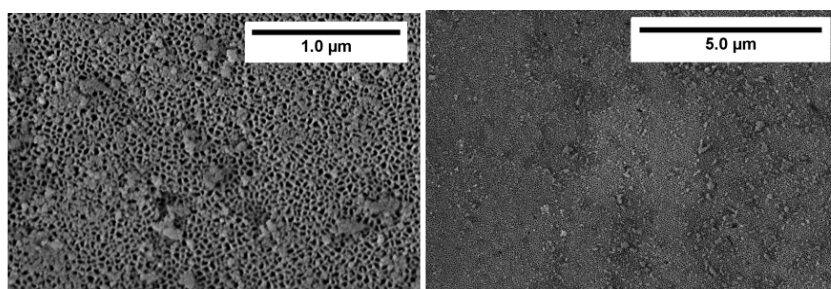**Figure 54. Ratio of Spreading Areas, D_i^2/D_f^2, vs. Droplet Volume of Hexadecane, DEP and TBP**

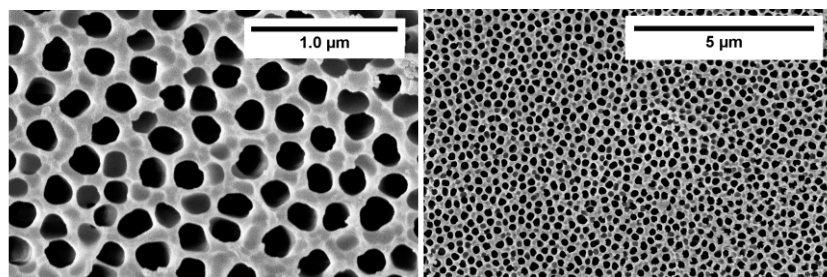**Figure 55. Type 1 Membrane, Top Side, Magnification of 45x, 11x**

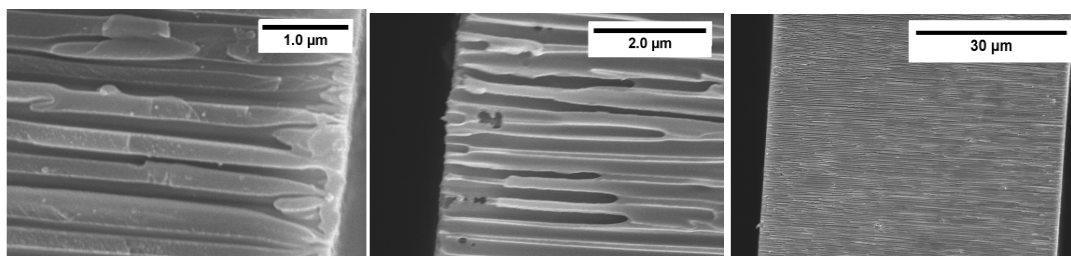**Figure 56. Type 1 Membrane, Bottom Side, Magnification 45x, 11x**

Figure 57. Side View on Type 1 Membrane, Magnification of 30x, 20x, and 1.8x

not go all the way through the membrane, and are inconsistent in length. What is most important is that the pore openings at the top side of Type 1 membrane are much smaller than those at the bottom side. Figure 58 shows that the bottom side type 1 forms a cupola under TBP and hexadecane after 2 min but no other droplets do. Figure 59 shows a magnified picture of the droplet contact line region. The terraces and precursors are clearly seen and one can notice that droplet spreading is caused by wicking of the liquid out of terraces into the pores. This observation suggests that the hierarchical pore structure of these membranes causes different distributions of the capillary pressure within the pore network. We hypothesize that the membrane side with
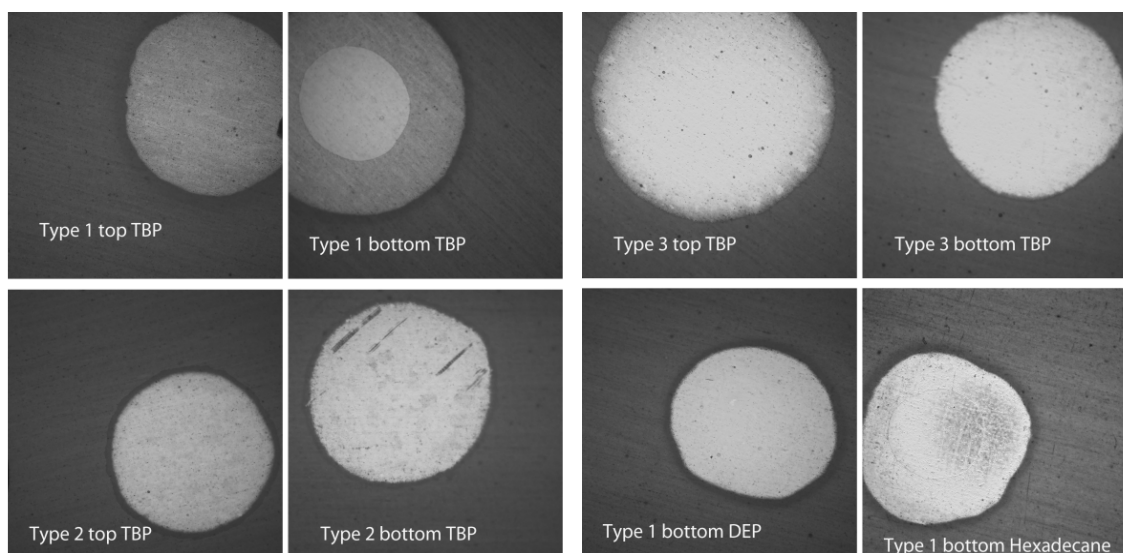

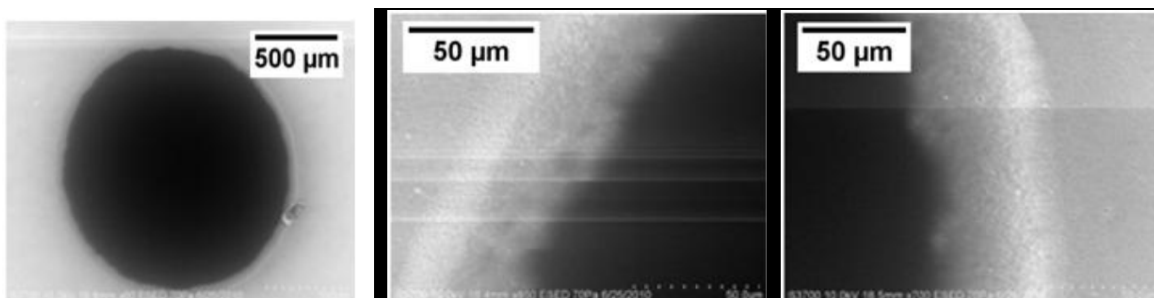**Figure 58. Droplet Morphology Taken after Two Minutes of Spreading**

Figure 59. SEM Images of TBP Droplet on Top Side of the Type 1 Membrane
(Courtesy of Dr. Stephanie Smith)

smaller pore openings would suck the liquid in, causing a collection of a liquid in a form of film biased to the side with smaller pore openings, where the capillary pressure is greater.

To estimate the thickness of the film trapped inside the membranes, we estimated the porosity of each membrane with the ImageJ (NIH) software. The porosity ε varied between 0.47–0.52, with the average $\varepsilon = 0.5$. Knowing the initial volume of the droplet (V_0), and the spreading area of the droplet, $A_f = \pi D_f^2/4$, we calculated the thickness of the trapped film h_{lc} as

$$V_0 = \varepsilon A_f h_{1c} \rightarrow V_0/\varepsilon A_f$$

The calculated thickness for different types of membranes is shown in Figures 60 and 61. The calculated thickness seems reasonable, except for one case, for which the droplet probably did not spread completely.
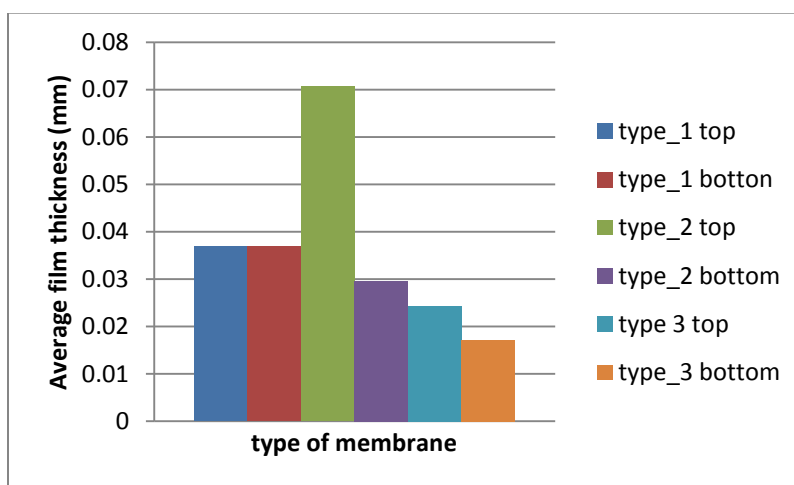
Figure 60. Average Film Thickness for Different Types of Membranes
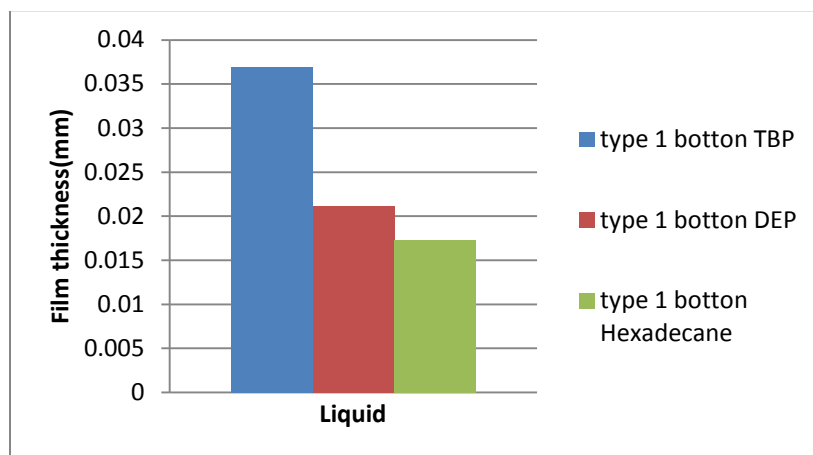
Figure 61. The Film Thickness of Different Liquids on Type 1 Membrane

Raman microanalysis has been used to confirm the hypothesis of trapped films. The spectra were taken at different points in each terrace (Fig.62b, dots 0–5). Each dotted location on Figure 62b is represented as a spectrum on Figure 63, in which the color legend is the same.

According to the spectral data, the TBP peak is present at points 0–2 and disappears at point 3. Figure 64 shows that intensity of the signal does change from point 1 to point 2.

Figure 62. Raman Microscope Image of Type 1 with Points Where the Spectra Were Taken

Figure 63. Raman Spectra Taken at Points Shown in Figure 62b; 820–879 cm^{-1} Signal Corresponds to TBP Peak in Raman Spectra on Type 1 Membrane

At point 0 we still have a cupola. Even though visually we can see differences between points 4 and 3 and background point 5, in the three spectra we cannot see a TBP signal. This observation suggests that the film is most l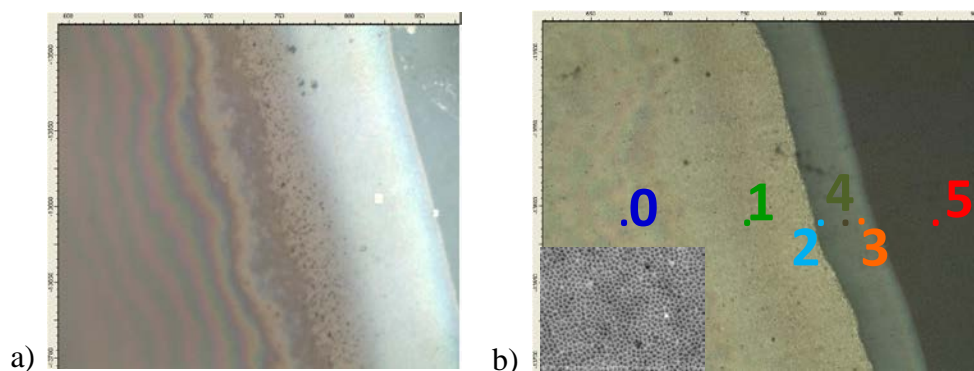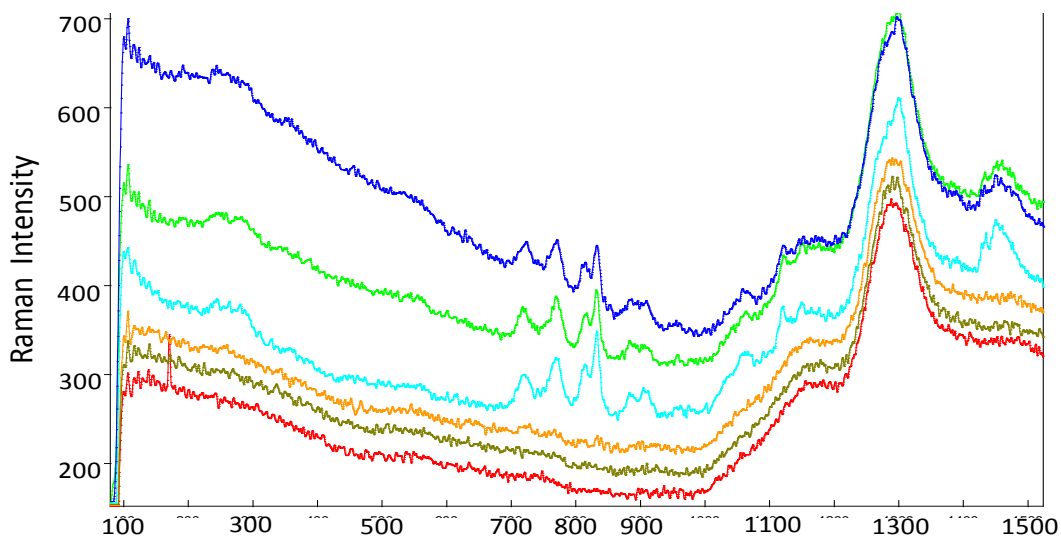ikely present inside the membrane and Raman cannot analyze it. Another explanation might be that the concentration of the TBP on the surface is below detection limit for this particular Raman spectrophotometer. We also examined the fate of the droplet after 12 or more hours. Figure 65 is a top view of the drop on the membrane after 14 hours.

In Figure 65 we were able to detect the TBP signal only at the center of the droplet, where the concentration of the liquid was highest. On the other hand, the microscopic image of this drop shows visible Newtonian rings, suggesting that a variable thickness of liquid is present inside the membrane.

In contrast, the TBP drop on the atomically smooth wafer covered with aluminum does not show any terraces, and only Newtonian rings are visible. This observation suggests that TBP is most likely trapped inside the membrane.

a)
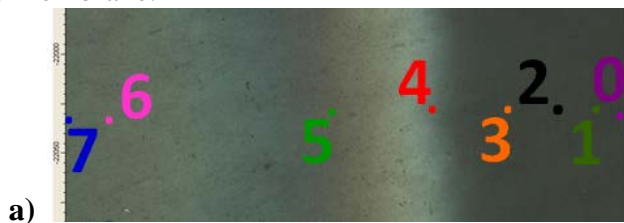
b)

Figure 64. a) Raman Microscope Image of Type 1 Showing Points Where the Spectra Were Taken b) Raman Spectra Taken in Points Numbered in a)
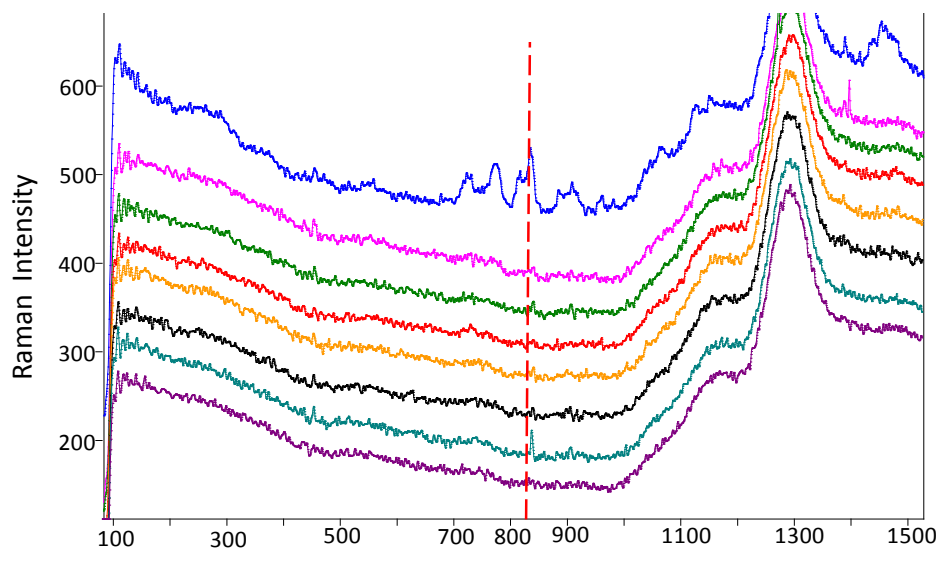

a)

b)
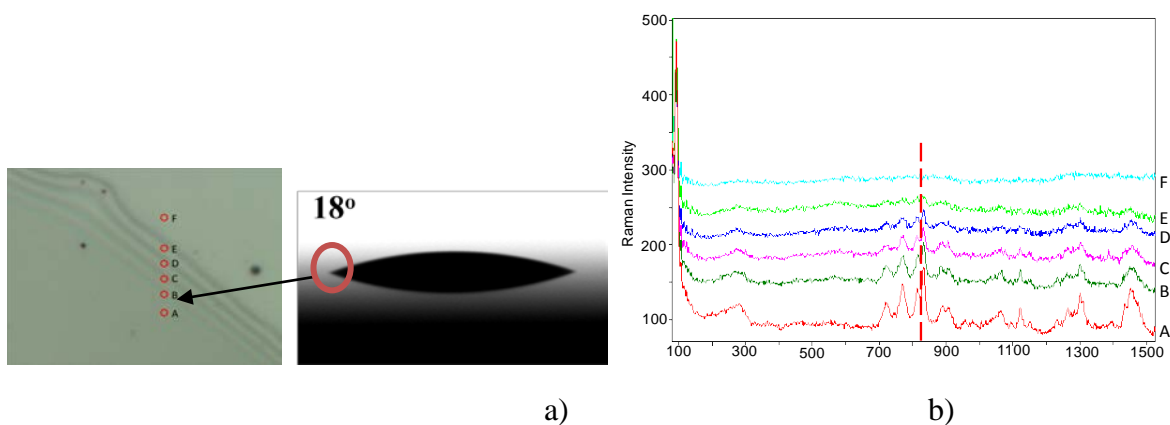
Figure 65. a) TBP Droplet on the Atmomically Smooth Wafer Covered with Aluminum and Contact Angle of TBP on the Aluminum Membrarne; b) Raman Spectra Taken at the Points Shown in a)

5. CONCLUSIONS

- LSE coatings based on industrial polyurethane materials were created
- Fluorinated silanes or perfluorocarboxylic acids were used to lower the surface energy of the coatings
- Addition of inorganic nanoparticles increases roughness of the coatings, decreasing effective surface energy for the surfaces treated with fluorochemicals
- For 67% titania-filled coatings apparent surface energy based on water and hexadecane CAs was calculated to be less than 2.24 mJ/m^2. When corrected for Wenzel roughness surface energy appeared to be 6.35 mJ/m^2
- For TiO_2-filled coatings CAs for MS were determined to be lower than the angles for CEES. CA for CEES was ~ 112°, and on the similar surface CA for MS was ~ 53°.
- Long (C_{12}) perfluorocarboxylic acids provide lower surface energy values than corresponding silane-treated coatings
- Polymer patches with relatively high surface energies deposited on top of fluorinated coatings are able to arrest movement of and swell with hexadecane and TBP
- Robustness of the PFDOA-treated PGMA coatings was tested. Increasing PFDOA treatment time from 1 to 4 h causes coatings to become softer and their uniformity to decrease. A TBP CA of ~80° was observed on a flat surface.
- PGMA was modified with PFDOA in solution and graft-copolymers (F-PGMA) obtained therefrom were used to modify model Si wafer surfaces. The surface energy of all samples was found to be close to or higher than 27.5 mN/m, the surface energy of hexadecane.
- Coatings were prepared with addition of either TiO_2 or $AlO(OH)$ or $Mg(OH)_2$ nanoparticles at different ratios. Nanoparticle addition to the PGMA treated with PFDOA led to increased coating roughness and a substantial drop in surface energy.
- Coatings with nanoparticles demonstrated very low calculated surface energy in the range of 1.1–2 mN/m. TBP, which was used as a CWA simulant in our studies, demonstrates very high CAs on these coatings, reaching values of ~128°.
- The type 1 bottom side membranes demonstrated unexpected $t^{1/2}$ kinetics of droplet spreading. TBP and hexadecane demonstrated similar square-root-of-time kinetics on this membrane, whereas DEP followed Tanner's kinetics.
- Other membrane types showed Tanner's law for drop–substrate interaction. We studied the mechanism of such a spreading and proposed a hypothesis that the pore hierarchy found in Type 1 membranes cause the droplet to follow the square root of time kinetics. Significantly different capillary pressures at opposite sides of the membrane pull the liquid to the side where the pore openings are smaller. As a result, the liquid was collected inside the membrane and formed a film. The results of optical microscopy, SEM, and Raman spectroscopy favor this hypothesis.

6. REFERENCES

1. Tsyalkovsky, V.; Klep, V.; Ramaratnam, K.; Lupitskyy, R.; Minko, S.; Luzinov, I., Fluorescent reactive core-shell composite nanoparticles with a high surface concentration of epoxy functionalities. *Chemistry of Materials* **2008,** *20* (1), 317-325.

2. Van Krevelen, D. W., *Properties of Polymers. Correlations with Chemical Structure*. 1st ed.; Elsever Publishing Company: Amstredam,London,New York, 1972; p 427.

3. Carroll, B. J., The Accurate Measurement of Contact Angle, Phase Contact Areas, Drop Volume, and La Place Excess Pressure in Drop-Fiber Systems. *Journal of Colloid and Interface Science* **1976,** *57* (3), 488-95.

4. Kamusewitz, H.; Possart, W., Wetting and scanning force microscopy on rough polymer surfaces: Wenzel's roughness factor and the thermodynamic contact angle. *Applied Physics a-Materials Science & Processing* **2003,** *76* (6), 899-902.

5. Starov, V. M.; Zhdanov, S. A.; Kosvintsev, S. R.; Sobolev, V. D.; Velarde, M. G., Spreading of liquid drops over porous substrates. *Advances in Colloid and Interface Science* **2003,** *104*, 123-158.

LIST OF SYMBOLS, ABBREVIATIONS, AND ACRONYMS

AFM	atomic force microscope
AFRL	Air Force Research Laboratory
CA$_{Hex}$	contact angle with hexadecane droplet
CA$_W$	contact angle with water droplet
CEES	2-chloroethyl ethyl sulfide
CWA	chemical warfare agent
DEP	diethyl phthalate
E	Young's modulus (of coatings)
F-PGMA	graft copolymer of PFDOA onto PGMA
FV	force volume (mode of the atomic force microscope)
LSE	low surface energy
MEK	methyl ethyl ketone
MS	methyl salicylate
PAA-POEGMA	polyacrylic acid-co-poly(oligoethylene glycol methacrylate)
PBMA	poly(butyl methacrylate)
PD-TDES	commercial mixture of perfluorododecyl- and perfluorotetradecyl-1H,1H,2H,2H-triethoxysilanes
PFDOA	perfluorododecanoic acid
PFHXA	perfluorohexanoic acid
PFTMHA	perfluoro-3,5,5-trimethylhexanoic acid
PGMA	poly(glycidyl methacrylate)
PTBA	poly(*tert*-butyl acrylate)
PTS	1H,1H,2H,2H-perfluorodecyltrimethoxysilane
PU	polyurethane
R	drop base radius,
RMS	root mean square
RW	two-component polyurethane resin topcoat
r^W	Wenzel roughness factor
SEM	scanning electron microscopy
SPM	scanning probe microscopy
TBP	tributyl phosphate
γ_s	surface energy
γ_s^d	dispersive component of surface energy
γ_s^p	polar component of surface energy
θ	contact angle with the surface